Bursting at the seams: the star-forming main sequence and its scatter at $z = 3$–9 using NIRCam photometry from JADES

C. Simmonds [1,2]★ S. Tacchella [1,2]★ W. McClymont [1,2] E. Curtis-Lake [3] F. D'Eugenio,[1,2]
K. Hainline,[4] B. D. Johnson,[5] A. Kravtsov [6,7,8] D. Puskás [1,2] B. Robertson,[9] A. Stoffers,[1,2]
C. Willott,[10] W. M. Baker,[11] V. A. Belokurov,[12] R. Bhatawdekar,[13] A. J. Bunker,[14] S. Carniani,[15]
J. Chevallard,[14] M. Curti,[16] Q. Duan,[1,2] J. M. Helton,[4] Z. Ji,[4] T. J. Looser,[5] R. Maiolino,[1,2,17]
M. V. Maseda,[18] I. Shivaei[19] and C. C. Williams[20]

Affiliations are listed at the end of the paper

ABSTRACT

We present a comprehensive study of the star-forming main sequence (SFMS) and its scatter at redshifts $3 \leq z \leq 9$, using Near Infrared Camera (NIRCam) photometry from the JADES (*JWST* Advanced Deep Extragalactic Survey) survey in the Great Observatories Origins Deep Survey (GOODS) South (GOODS-S) and North (GOODS-N) fields. Our analysis is based on a sample of galaxies that is stellar mass complete down to $\log(M_\star/M_\odot) \approx 8.1$. The redshift evolution of the SFMS at an averaging time-scale of 10 Myr follows a relation, quantified by the specific star formation rates (sSFR$_{10}$), of sSFR $\propto (1+z)^\mu$ with $\mu = 2.30^{+0.03}_{-0.01}$, in good agreement with theoretical predictions and the specific mass accretion rate of dark matter haloes. We find that the SFMS normalization varies in a complex way with the SFR averaging time-scale, reflecting the combined effects of bursty star formation and rising star formation histories (SFHs). We quantify the scatter of the SFMS, revealing that it decreases with longer SFR averaging time-scales, from $\sigma_{int} \approx 0.4 - 0.5$ dex at 10 Myr to $\sigma_{int} \approx 0.2$ dex at 100 Myr, indicating that shorter term fluctuations dominate the scatter, although long-term variations in star formation activity are also present. Our findings suggest that bursty SFHs are more pronounced at lower stellar masses. Furthermore, we explore the implications of our results for the observed overabundance of UV-bright galaxies at $z > 10$, concluding that additional mechanisms, such as top-heavy initial mass functions, increased star formation efficiencies, or increased burstiness in star formation are needed to explain these observations. Finally, we emphasize the importance of accurate stellar mass completeness limits when fitting the SFMS, especially for galaxies with bursty SFHs.

Key words: galaxies: evolution – galaxies: general – galaxies: star formation.

1 INTRODUCTION

The cosmic star formation history (SFH) traces the evolution of the star formation rate (SFR) density across cosmic time, capturing the collective star formation activity of all galaxies from a few million years after the big bang to the present, with a peak at redshift $z \approx 2$ (see P. Madau & M. Dickinson 2014, and references within). While this global history provides critical insight into the overall star formation process in the Universe, the SFHs of individual galaxies reveal the underlying physical mechanisms driving galaxy formation and evolution. These individual histories vary significantly, reflecting the complex interplay between gas accretion, star formation, and feedback processes (A. Dekel et al. 2013; S. Tacchella et al. 2016a; K. G. Iyer et al. 2020; W. McClymont et al. 2025a). Understanding how these diverse SFHs contribute to the cosmic SFR density is key to unravelling the detailed processes of galaxy assembly over time.

An important scaling relation to study SFHs of galaxies is the star-forming main sequence (SFMS), which is the tight relation between SFR and stellar mass that has been widely established for star-forming galaxies up to $z \sim 3$ (including, but not limited to J. Brinchmann et al. 2004; N. A. Reddy et al. 2006; E. Daddi et al. 2007; K. G. Noeske et al. 2007; S. Salim et al. 2007; K. E. Whitaker et al. 2012; J. S. Speagle et al. 2014; P. Popesso et al. 2023). The SFMS is usually described as a linear relation in logarithmic space between SFR (or specific SFR; sSFR≡SFR/$M_\star$) and stellar mass ($M_\star$). On average, studies show that at fixed $M_\star$, SFR (and sSFR) increase as a function of redshift, although we note that the specific shape of this relation highly depends on the sample selection and the techniques used to estimate SFRs (A. Katsianis, E. Tescari & J. S. B. Wyithe 2016; L. J. M. Davies et al. 2019). With a relatively narrow SFMS scatter of $\sigma \approx 0.3$ dex, the increase in SFMS normalization from $z \approx 0$ to ≈ 3 can be primarily attributed to higher gas fractions in galaxies, with star formation efficiency and galaxy–galaxy mergers playing subdominant roles in driving higher SFRs (N. Bouché et al.

2010; E. Daddi et al. 2010; G. Rodighiero et al. 2011; L. J. Tacconi, R. Genzel & A. Sternberg 2020).

Although several studies have demonstrated the presence of the SFMS extending to the Epoch of Reionization (EoR; $z \approx 5-9$; E. Daddi et al. 2010; J. S. Speagle et al. 2014; B. Salmon et al. 2015; C. Schreiber et al. 2015; L. A. M. Tasca et al. 2015; P. Santini et al. 2017; P. Popesso et al. 2023), until the advent of the *James Webb Space Telescope* (*JWST*) its exact shape and scatter remained uncertain due to the observational limitation of mainly probing the rest-frame ultraviolet (UV) emission at these redshifts. Theoretically, the SFMS at $z = 3-9$ is predicted by simple models of galaxy formation, where the SFRs of galaxies are closely tied to dark matter accretion (A. Rodríguez-Puebla et al. 2016; S. Tacchella et al. 2018). The key insight, however, comes from examining the distribution of galaxies around the SFMS, characterized by its scatter, as this encodes the underlying physical processes driving star formation on global (M. D. Gladders et al. 2013; L. E. Abramson et al. 2014; D. D. Kelson 2014; S. Tacchella et al. 2016a; N. Caplar & S. Tacchella 2019; J. Matthee & J. Schaye 2019; K. G. Iyer et al. 2020; E. Wang & S. J. Lilly 2020; J. T. Wan et al. 2025; W. McClymont et al. 2025a) and spatially resolved scales, giving rise to bulges and discs (A. Zolotov et al. 2015; S. Tacchella et al. 2016b; S. Appleby et al. 2020; N. Emami et al. 2021; P. F. Hopkins et al. 2023; S. Lapiner et al. 2023; E. Cenci et al. 2024; W. McClymont et al. 2025b).

Burstiness – the variability of the SFR on short time-scales (relative to the dynamical time-scale of galaxies, e.g. a few tens of Myr) – is predicted to increase toward lower mass galaxies and higher redshifts. In low-mass ($M_\star < 10^9 \, \mathrm{M_\odot}$) galaxies, bursty star formation potentially arises from episodic stellar feedback processes that expel gas from the interstellar medium (ISM; P. F. Hopkins et al. 2014; C. C. Hayward & P. F. Hopkins 2017; P. F. Hopkins et al. 2023; T. Dome et al. 2024), as well as from environmental effects such as galaxy–galaxy interactions (P. Di Matteo et al. 2007; R. Teyssier, D. Chapon & F. Bournaud 2010; Y. Asada et al. 2024; Q. Duan et al. 2024). At higher redshifts, burstiness is expected across all galaxy masses and is likely due to highly variable gas accretion and short equilibrium time-scales (D. Anglés-Alcázar et al. 2017; C.-A. Faucher-Giguère 2018; S. Tacchella, J. C. Forbes & N. Caplar 2020; T. J. Looser et al. 2025; W. McClymont et al. 2025a).

While burstiness can be easily measured and quantified in theoretical models, where the evolution of individual galaxies can be traced, observational studies must rely on proxies to assess this phenomenon, as SFHs cannot be measured at arbitrarily short time-scales over large lookback times. However, two empirical estimates of SFRs are known to gauge two specific time-scales. The Hα emission line traces ionizing radiation from massive, short-lived stars, therefore probing SFRs on time-scales of $\approx 5-10$ Myr, while the UV continuum probes SFRs on time-scales of $\approx 10-50$ Myr (R. C. Kennicutt & N. J. Evans 2012). These tracers have been used to demonstrate that lower mass galaxies tend to have burstier SFHs (D. R. Weisz et al. 2012; K. Guo et al. 2015; N. Emami et al. 2019; K. Boyett et al. 2024; D. Langeroodi & J. Hjorth 2024; T. J. Looser et al. 2025). Burstiness has also a direct impact on the SFMS: more bursty SFHs lead to an increase of the SFMS normalization (N. Caplar & S. Tacchella 2019; M. Donnari et al. 2019a) and a decrease of the SFMS scatter when longer time-scale SFR indicators are used (S. Tacchella et al. 2020; J. T. Wan et al. 2025). Recently, Bayesian hierarchical models have also been explored as a way to infer burstiness from individual and an ensemble of galaxies through spectral energy distribution (SED) modelling (J. T. Wan et al. 2024; C. Carvajal-Bohorquez et al. 2025; J. T. Wan et al. 2025).

Ever since its launch, *JWST* has given us an unprecedented view of the early Universe (J. P. Gardner et al. 2023). To name a few of its advantages that are relevant to this work, it has granted us access to rest-frame optical wavelengths at $z > 6$, allowed us to improve SFR indicators through measurements of the Balmer lines (e.g. Hα and Hβ), and provided us with data to obtain more accurate stellar masses, resulting in updated measurements of the SFMS (L. Clarke et al. 2024; J. W. Cole et al. 2025; P. Rinaldi et al. 2025). Importantly, *JWST* has unveiled an intriguing population of galaxies at $z > 10$, which are UV-brighter and more numerous than predicted (e.g. R. P. Naidu et al. 2022; S. L. Finkelstein et al. 2023; B. E. Robertson et al. 2023; S. Carniani et al. 2024; K. N. Hainline et al. 2024; B. Robertson et al. 2024; V. Kokorev et al. 2025; R. P. Naidu et al. 2025; A. Weibel et al. 2025; L. Whitler et al. 2025). One key avenue to explore in this context, is how bursty SFHs affect – and possibly explain – the observed UV luminosity functions at $z > 10$ (X. Shen et al. 2023; G. Sun et al. 2023b; A. Kravtsov & V. Belokurov 2024), specifically, the overabundance of UV-bright galaxies detected with *JWST* in the past years.

In addition to possibly explaining the puzzling observations at $z > 10$, quantifying the burstiness of SFHs has important astrophysical implications at lower redshifts. For example, it can shed light on the sources responsible for ionizing the Universe during the EoR. This period of time represents the transition between a dark and neutral IGM to a fully ionized one by $z \sim 5-6$ (L. C. Keating et al. 2020; S. E. I. Bosman et al. 2022; Y. Zhu et al. 2024). Star-forming galaxies are believed to have played a crucial role in the ionization of the Universe, due to the copious amounts of Lyman continuum radiation (photons with $\lambda < 912$ Å, or $E > 13.6$ eV) produced by their young massive stars (S. Hassan et al. 2018; J. Rosdahl et al. 2018; M. Trebitsch, M. Volonteri & Y. Dubois 2020). Moreover, in the context of star-forming galaxies as main agents of reionization, many studies suggest low-mass galaxies with bursty star formation are the dominant source of ionizing photons (e.g. R. Endsley et al. 2023; J. Y. C. Yeh et al. 2023; P. Rinaldi et al. 2024; C. Simmonds et al. 2024a). However, it must be noted that recent observations obtained with the *JWST* have reignited the debate regarding the contribution arising from active galactic nuclei (AGNs; see e.g. A. Grazian et al. 2024; P. Madau et al. 2024; R. Maiolino et al. 2024; S. Asthana et al. 2025). Therefore, understanding the interplay between stellar mass and star formation as a function of redshift can help unveil the sources of reionization.

Two important questions that arise from the study of the SFMS are: (1) how universal is the SFMS at early times? and, (2) what processes govern its emergence and evolution? In this work, we aim to answer these questions by measuring the shape, scatter, and normalization of the SFMS for galaxies at $z = 3-9$ using *JWST* Near Infrared Camera (NIRCam) photometry from the *JWST* Advanced Deep Extragalactic Survey (JADES; D. J. Eisenstein et al. 2023a; A. J. Bunker et al. 2024; F. D'Eugenio et al. 2025), combined with SED fitting using PROSPECTOR. We focus on galaxies at $z = 3-9$, where rest-frame optical data are accessible in addition to the UV, enabling robust constraints on stellar masses and SFRs. This is in stark contrast to studies at $z > 9$, which typically rely mostly on rest-frame UV photometry and may overestimate the intrinsic scatter in SFR due to larger measurement uncertainties. Moreover, our use of deep JADES photometry (including medium-band data when available) avoids the selection biases and limited completeness inherent in spectroscopic samples, which are affected by strong emission-line flux cuts and complex targeting strategies. The structure of this work is the following. In Section 2, we discuss the data and sample selection used in this work. We then estimate galaxy properties using

the SED-fitting code PROSPECTOR in Section 3, and analyse the stellar mass completeness of our sample. In Section 4, we present our best-fit to the SFMS at $3 < z < 9$, and compare it to estimations from the literature. In Section 5, we measure the scatter of the SFMS as a function of redshift, stellar mass, and averaging time-scales. We then use our results to make conclusions about the burstiness of star formation in the galaxies here studied. We explore the implications of our findings in the context of observations of the early Universe in Section 6. Finally, we consider the caveats and limitations of our work in Section 7, ending with concluding remarks in Section 8. Throughout this work, we assume $\Omega_0 = 0.315$ and $H_0 = 67.4$ km s^{-1} Mpc^{-1}, following Planck Collaboration VI (2020).

2 DATA AND SAMPLE SELECTION

In this section, we briefly describe the observations used in this work, as well as the selection criteria for our sample.

2.1 Observations

We make use of the full JADES (D. J. Eisenstein et al. 2023a; A. J. Bunker et al. 2024) photometry set in both the Great Observatories Origins Deep Survey (GOODS) North (GOODS-N) and South (GOODS-S) regions (M. Giavalisco et al. 2004), including the publicly available NIRCam Deep imaging (M. J. Rieke et al. 2023), and the JADES Origins Field (JOF; D. J. Eisenstein et al. 2023b). When available, we also use photometry from the *JWST* Extragalactic Medium-band Survey (JEMS; C. C. Williams et al. 2023), and from the First Reionisation Epoch Spectroscopic Complete Survey (FRESCO; P. A. Oesch et al. 2023). In addition to the photometric catalogues, we use emission-line fluxes derived from spectroscopic observations to compare to fluxes inferred from SED fitting. Specifically, in Section 3.1, we compare our PROSPECTOR-inferred fluxes of Hα and [O III]$_{\lambda 5007}$ to those obtained by JADES using the *JWST* microshutter assembly of NIRSpec (P. Ferruit et al. 2022; P. Jakobsen et al. 2022; A. J. Bunker et al. 2024; F. D'Eugenio et al. 2025).

For the GOODS-S region, we rely on the same photometric catalogues as in C. Simmonds et al. (2024a, b). In this work, however, we also include catalogues produced in the same fashion for the GOODS-N region. Briefly, the source detection and photometry was performed on JEMS NIRCam medium-band and JADES NIRCam broad- and medium-band imaging, using the PHOTUTILS software package (L. Bradley et al. 2022). Sources with five or more contiguous pixels of the SNR (signal-to-noise ratio) mosaic with signal $> 3\sigma$ were identified. Furthermore, PHOTUTILS was used to perform circular aperture photometry with filter-dependent aperture corrections based on model point spread functions following the method presented in Z. Ji et al. (2024), as described in B. Robertson et al. (2024). In addition to the NIRCam observations, *Hubble Space Telescope* (*HST*) images released through the Hubble Legacy Field program (G. Illingworth et al. 2016; K. E. Whitaker et al. 2019) reductions of GOODS-S and GOODS-N (M. Giavalisco et al. 2004) and Cosmic Assembly Near-infrared Deep Extragalactic Legacy Survey (N. A. Grogin et al. 2011; A. M. Koekemoer et al. 2011) images. In this work, we adopt a Kron aperture on images, convolved to a common resolution, and impose an error floor of 5 per cent in each band.

2.2 Sample selection criteria

For this work, we use PROSPECTOR-inferred properties as described in C. Simmonds et al. (2024b) for galaxies in GOODS-S, but extended

to include galaxies in GOODS-N. Out of the full JADES photometry data set, we only impose the following conditions: (1) sources must have an SNR$\geq$3 in the $F444W$ band, (2) a median PROSPECTOR-derived redshift in the range $z_{\rm phot} = 3 - 9$, and (3) a reduced $\chi^2 \leq 10$ to remove objects with catastrophically bad fits. Finally, we remove the *JWST* Mid-Infrared Instrument (MIRI) selected AGN from J. Lyu et al. (2024) and the broad-line AGN from I. Juodžbalis et al. (2025).[1] This sample selection criteria yields 29 220 galaxies in GOODS-S, and 18 936 galaxies in GOODS-N, resulting in a total sample of 48 156 galaxies. Out of the total sample, 99 per cent (91 per cent) of the galaxies have medium-band coverage in at least one (two) photometric band(s).

3 ESTIMATION OF GALAXY PROPERTIES

This work uses galaxy properties derived from the SED modelling code PROSPECTOR, specifically, we infer stellar masses, SFRs across different time-scales, and UV magnitudes. In this section, we outline the SED modelling procedure, how SFRs are estimated, and the stellar mass completeness of our sample. SED modelling offers a more robust estimation of SFRs compared to direct tracers like UV and Hα, as it incorporates a galaxy's full SED, accounting for systematic errors that may arise from variations in dust attenuation (including variations in the dust attenuation law), complex SFHs, and nebular continuum and line emission. While UV and Hα tracers are affected by factors such as dust attenuation and metallicity (e.g. through their impact on conversion factors), they often provide limited insight into the full SFH, especially since they trace specific time-scales. For example, Hα is insensitive to time-scales larger than a few tens of million years, as it is a tracer of instantaneous star formation. In contrast, SED modelling with sufficient spectral coverage, resolution, and sensitivity enables a self-consistent analysis that mitigates systematic biases and yields a more accurate view of star formation across time-scales, particularly at high redshift, by properly accounting for parameter degeneracies and uncertainties.

3.1 SED fitting with PROSPECTOR

In this work, we use the SED-fitting code PROSPECTOR (B. D. Johnson et al. 2019, 2021) to derive galaxy properties. The fitting routine used to fit our entire sample is described in C. Simmonds et al. (2024b). Briefly, we use photometry from the full JADES photometric catalogues as input for PROSPECTOR, including data from the UV to the IR from *HST* and *JWST* NIRCam (see fig. 1 from C. Simmonds et al. 2024b). We adopt the same Kron convolved aperture to extract *HST*, JADES, and JEMS photometry, and floor the photometric errors to 5 per cent to account for systematic errors not accounted for by our data reduction pipelines. We use photometric redshifts ($z_{\rm phot}$) inferred with the SED template-fitting code EAZY (G. B. Brammer, P. G. van Dokkum & P. Coppi 2008) as priors in our SED-fitting routine. As shown in M. J. Rieke et al. (2023) and K. N. Hainline et al. (2024), $z_{\rm phot}$ can be accurately determined when a rich photometry set is used. The dust attenuation and stellar population properties are varied following S. Tacchella et al. (2022b). Importantly, we use a two component dust model (S. Charlot & S. M. Fall 2000; C. Conroy, J. E. Gunn & M. White 2009), which accounts

---

[1]We note that these spectroscopically confirmed AGN represent <10 per cent of the entire sample of galaxies for which we have spectra. Moreover, they are mostly composed of low-luminosity AGN, where it is likely that the continuum is dominated by the host galaxy.
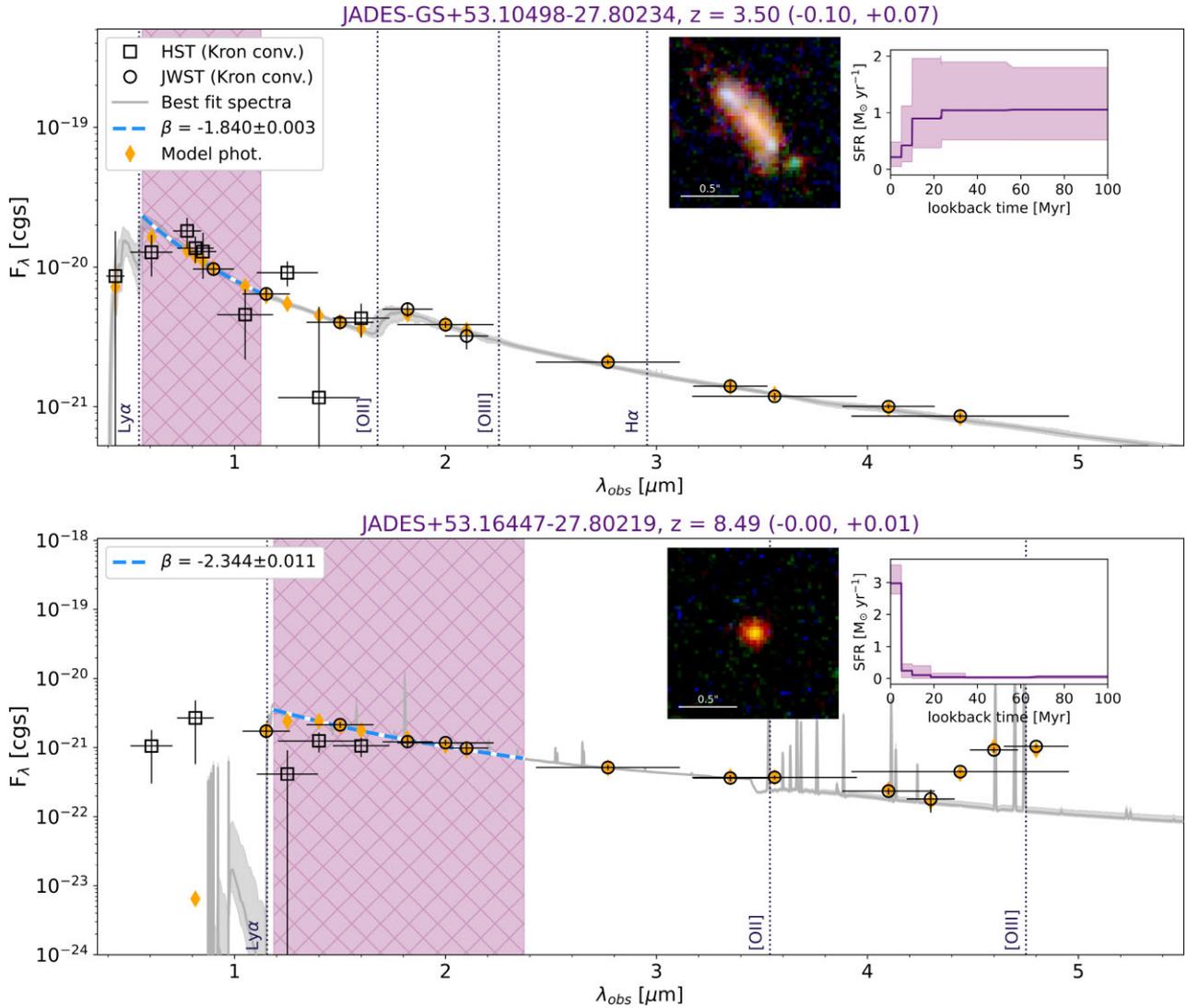
Figure 1. Representative examples of the products of our SED-fitting routine with PROSPECTOR. The names and redshifts for each galaxy are indicated in the titles. The names are composed by the coordinates of each galaxy rounded to the fifth decimal. The observed photometry is shown as open squares (*HST*) and circles (*JWST* NIRCam), while the best-fitting photometry is shown as orange diamonds, and the best-fitting spectra is shown in grey. We also show the UV continuum slope (β, given by $F_\lambda \propto \lambda^\beta$ D. Calzetti, A. L. Kinney & T. Storchi-Bergmann 1994), obtained by fitting a line to the best-fitting spectra in logarithmic space at $\lambda_{\rm rest-frame} = 1250 - 2500$ Å (purple hatched region). The vertical dotted lines show the expected wavelength of selected emission lines. Finally, the insets show the SFH and an RGB image of the selected galaxy. These examples illustrate the power of PROSPECTOR to reproduce the observed SED shapes of galaxies even in the absence of strong emission lines. Top panel: galaxy at $z \sim 3.5$ with no evidence of strong emission lines and a declining SFH. Bottom panel: galaxy at $z \sim 8.5$ with strong evidence of [O III]$_{\lambda 5007}$ and a recent burst in star formation.

for the differential dust attenuation in young (< 10 Myr) stars and nebular emission lines by using different optical depths and a variable dust index (M. Kriek & C. Conroy 2013). We adopt a Chabrier (G. Chabrier 2003) initial mass function (IMF) with mass cut-offs of 0.1 and 100 M$_\odot$, and allow the stellar metallicity to explore a range between 0.01 and 1 Z$_\odot$. The continuum and emission properties of the SEDs are provided by the Flexible Stellar Population Synthesis (FSPS) code (C. Conroy & J. E. Gunn 2010), based on CLOUDY (v13.03; G. J. Ferland et al. 2013) using MESA Isochrones & Stellar Tracks (J. Choi et al. 2016; A. Dotter 2016), and the MILES stellar library (A. Vazdekis et al. 2015). The UV extension of the latter is based on the Basel Stellar Library (E. Lastennet et al. 2002). The use of this CLOUDY grid results in a limitation of the maximum permitted ionization parameter of $\log\langle U\rangle_{\rm max} = -1.0$, which might not be enough to reproduce the properties of some high-redshift galaxies (e.g. A.

J. Cameron et al. 2023). We set a flexible IGM model based on a scaling of the Madau model (P. Madau 1995), where the scaling is left as a free parameter. Finally, we use a non-parametric SFH (continuity SFH; J. Leja et al. 2019). In this model, the SFH is described as eight different SFR bins. The minimum bin is set to a lookback time of $1 - 5$ and $5 - 10$ Myr, while the rest are divided equally in logarithmic space depending on the redshift. The ratios and amplitudes of the bins are allowed to vary following a Student's t-distribution with a width of 0.3. Importantly, this prior allows (but does not impose) a somewhat bursty SFH when the data favour it.

To showcase the products of our SED-fitting process, in Fig. 1 we present two galaxies with significantly different SFHs at the limits of our redshift range. These are representative examples that highlight the power of PROSPECTOR when a comprehensive photometric set is used. In particular, they demonstrate how PROSPECTOR is able to fit
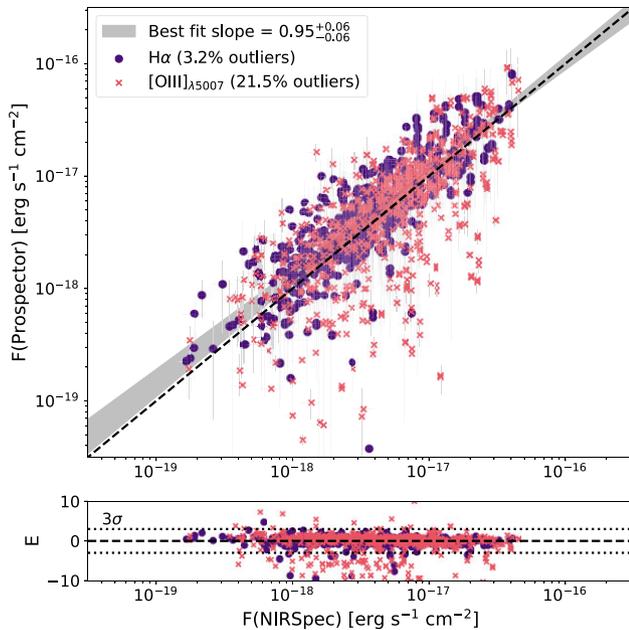
Figure 2. Comparison of PROSPECTOR-inferred Hα (circles) and [O III]$_{\lambda5007}$ (crosses) emission line fluxes to ones measured from JADES using NIRSpec. The bottom panel shows the difference between the inferred and measured values including their respective errors, given by: $E \equiv (F_{\mathrm{Prospector}} - F_{\mathrm{NIRSpec}})/(\sqrt{\sigma_{\mathrm{Prospector}}^2 + \sigma_{\mathrm{NIRSpec}}^2})$. The dotted lines denote the 3σ range, measurements outside of these limits are considered outliers. We find an outlier fraction of 3.2 per cent for Hα and 21.5 per cent for [O III]. Finally, the JADES measurements might be underestimated in bright galaxies due to slit losses. Overall, we find good agreement between our fitted values and the observed ones, as shown by the best fit to the data (shaded area).

the observed SED shapes even in the absence of strong emission lines (see also fig. A.2 of C. Simmonds et al. 2024b). Moreover, we find that PROSPECTOR can reproduce emission-line fluxes reasonably well for our sample based on photometry alone. In Fig. 2, we compare Hα and [O III]$_{\lambda5007}$ fluxes derived by PROSPECTOR to a subsample of galaxies with JADES NIRSpec observations (782 Hα and 887 [O III] flux measurements with SNR$\geq$ 5). Overall, we find good agreement between our SED-inferred fluxes and those measured by spectroscopic observations, with values scattering around the 1:1 line and outlier fractions of 3.2 per cent and 21.5 per cent for Hα and [O III], respectively. Therefore, we confirm that our SED-fitting routine can reproduce emission lines to a reasonable extent.

3.2 Stellar mass completeness

As in C. Simmonds et al. (2024b), we estimate the stellar mass completeness of our sample following the method described in section 5.2 of L. Pozzetti et al. (2010). To summarize, for every redshift a minimum mass (M_{min}) is defined, above which potentially all types of galaxies can be observed (i.e. not only those who have had a recent burst in star formation). To calculate M_{min}, the limiting stellar mass (M_{lim}) must be estimated. M_{lim} represents the stellar mass a galaxy would have if its apparent magnitude (m) were equal to the limiting magnitude of the survey (m_{lim}). Importantly, M_{lim} depends on the stellar mass-to-light ratio, a quantity that can be affected by bursty star formation (i.e. by galaxies being upscattered due to a recent burst in star formation). In this work, m_{lim} is determined by the $F444W$ band, since it has the highest effective wavelength, making it the best tracer of stellar mass available in our data, although we
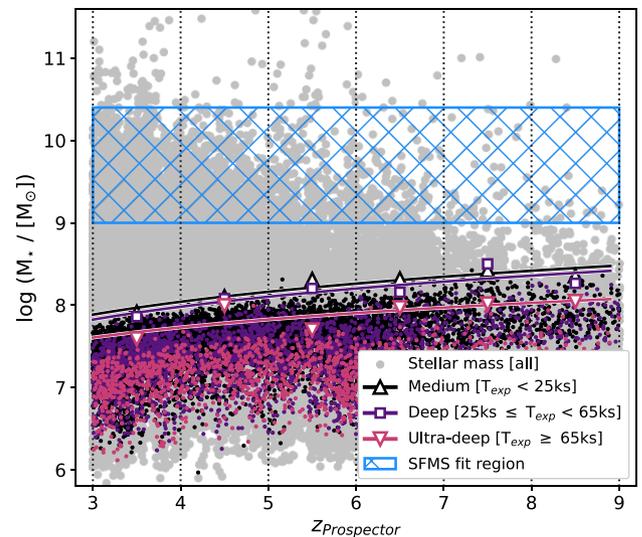
Figure 3. Stellar mass completeness of the sample, divided into three fields depending on exposure time (T_{exp}). The larger grey circles show the stellar mass of each galaxy as a function of redshift, while the smaller coloured circles show the limiting mass for the faintest 20 per cent. The solid curves denote the 100 per cent completeness at each redshift and for each depth, as indicated in the legend, following the prescription of L. Pozzetti et al. (2010). We find our sample is stellar mass complete down to $\log(M_\star/[\mathrm{M}_\odot]) \approx 8.1$ on average, with small variations depending on the depth of the field. The dotted vertical lines mark the redshift bins used in the mass completeness estimation. The blue hatched area shows the region used to fit the SFMS (i.e. $9.0 \leq \log(M_\star/\mathrm{M}_\odot) \leq 10.3$ and $3 \leq z \leq 9$).

caution that at $z > 5$, it is susceptible to strong emission line biases. For each galaxy, M_{lim} is given by:

$$\log(M_{\mathrm{lim}}) = \log(M_\star) + 0.4(m - m_{\mathrm{lim}}), \tag{1}$$

where $M_\star$ is stellar mass in units of solar masses. We divide our sample into three fields depending on their $F444W$ exposure time: medium ($T_{\mathrm{exp}} < 25$ ks), deep (25 ks $\leq T_{\mathrm{exp}} < 65$ ks), and ultradeep ($T_{\mathrm{exp}} \geq 65$ ks), with 5σ flux depths of 6, 4.5, and 2.65 nJy, respectively. In order to compute M_{min} for each field and at each redshift bin, we select the faintest 20 per cent of galaxies for each exposure time. This choice takes into account the colour–luminosity relation and therefore includes only galaxies with a typical M/L close to the magnitude limit.

In C. Simmonds et al. (2024b), we focused on galaxies above which 90 per cent of the selected M_{lim} lie, however, in this work we place a stricter limit of 100 per cent, because even a small incompleteness percentage can significantly bias estimates of average SFRs (J. Leja et al. 2022). The results are shown in Fig. 3, where the stellar mass as a function of redshift is shown for our full sample (grey circles), and the M_{lim} of the faintest 20 per cent of galaxies per T_{exp} are shown as coloured points. We find, on average, that our sample is stellar mass complete down to $\log(M_\star/\mathrm{M}_\odot) \approx 8.1$. We note that the method used here to establish the stellar mass completeness limits of our sample relies on the assumption of a constant mass-to-light ratio. If SFHs are bursty, it means that SFRs change on short time-scales, which results in a non-constant mass-to-light ratio in the ionizing (and to a lesser extent in the non-ionizing) continuum (A. Domínguez et al. 2015). Thus, if the galaxies in our sample have bursty SFHs, then the limits shown in Fig. 3 should be taken as lower limits, as will be discussed further in Section 6.2.

In the remainder of this work, we focus on galaxies with masses higher than the stellar mass completeness limit derived above of $\log(M_\star/M_\odot) \approx 8.1$, yielding a sample of 18 321 galaxies (~ 38 per cent of the total sample). However, we also present a more conservative stellar mass completeness limit motivated by the behaviour of the sSFR as a function of stellar mass (see Section 4), with $\log(M_\star/M_\odot) = 9.0$–10.3, shown as a blue hatched region in Fig. 3, containing 2989 galaxies.

3.3 Star formation rates

We have shown in Fig. 2 that PROSPECTOR can retrieve emission-line fluxes reasonably well. However, we decide against using SFR tracers derived from these lines (e.g. from Hα; R. C. Kennicutt 1998; J. Pflamm-Altenburg, C. Weidner & P. Kroupa 2009; R. C. Kennicutt & N. J. Evans 2012; S. Tacchella et al. 2022a; Kramarenko et al. (in preparation)) or from the UV luminosity due to their dependence on dust corrections, metallicity, and the parameter space on which the relations have been calibrated, both introducing additional uncertainties (R. C. Kennicutt & N. J. Evans 2012; R. Smit et al. 2016; E. Curtis-Lake et al. 2021; A. E. Shapley et al. 2023; D. Rosa-González, E. Terlevich & R. Terlevich 2002).[2] Moreover, SFR calibrations based on UV and IR luminosities have been shown to be systematically higher than SFRs inferred through SED fitting at a given stellar mass (A. E. Bauer et al. 2011), especially if the galaxies are quiescent (more than ~ 1 dex; C. C. Hayward et al. 2014; D. Utomo et al. 2014; J. Leja et al. 2022). This could be an indication of obscured star formation, which can be difficult to detect in the rest-frame UV and optical wavelength range (i.e. 'outshining'; C. Papovich, M. Dickinson & H. C. Ferguson 2001; C. Conroy 2013; K. E. Whitaker et al. 2017; C. Papovich et al. 2023; F. Sun et al. 2024; C. C. Williams et al. 2024; T. Herard-Demanche et al. 2025; N. A. Reddy et al. 2025). Quantifying this effect on our sample is beyond the scope (and limitations) of this work, however, future surveys with *JWST* MIRI are a promising avenue to explore this problem further (J. M. Helton et al. 2025a). In addition to dust corrections and conversions between luminosity and SFRs, this discrepancy can be explained by older stellar populations contributing to the UV and IR regions of galaxy SEDs, and is more significant in the absence of young stellar populations (i.e. a recent star burst). Therefore, in this work, we rely on the SFRs provided by PROSPECTOR at different averaging time-scales, as they offer a more comprehensive estimation by incorporating a galaxy's full SED, including dust attenuation, SFHs, and nebular emission. This approach reduces the systematic biases associated with direct tracers like UV and Hα, and allows for a self-consistent analysis across multiple time-scales, which is particularly important when studying galaxies at high redshifts where such tracers may be affected by additional complexities.

Specifically, we use the SFRs averaged over the past 10, 20, 30, 40, 50, and 100 Myr (indicated by the subscript of the SFR used). These SFR can be estimated largely independent given the time bins in our SFH modelling, e.g. any covariance between these SFRs can be attributed physical processes that drive star formation. These values are obtained by integrating the SFHs and dividing them by the stellar mass formed at each time-scale. The self-consistency provided by the PROSPECTOR modelling imposes a natural maximum in sSFR given by $\frac{1}{t_{\rm average}}$. Studying different time-scales of star formation

---

[2]We note that SFR$_{10}$ and SFR$_{\rm H\alpha}$ largely agree for galaxies in our sample, both when PROSPECTOR-inferred and NIRSpec measured Hα fluxes are used (see Appendix A).

for a given galaxy informs us about the burstiness of its SFH. In particular, the ratio between the star formation averaged over two different time-scales (i.e. SFR$_{10}$/SFR$_{50}$ or SFR$_{10}$/SFR$_{100}$) contains information about the fluctuations in star formation over time (D. R. Weisz et al. 2012; Y. Guo et al. 2016; N. Caplar & S. Tacchella 2019; L. Clarke et al. 2024; J. W. Cole et al. 2025).

4 FITTING THE STAR-FORMING MAIN SEQUENCE

The SFMS describes the relation between SFR (or sSFR) and stellar mass, and has been extensively studied up to $z \sim 6$ (J. Brinchmann et al. 2004; E. Daddi et al. 2007, 2022; D. Elbaz et al. 2007, 2011; S. Salim et al. 2007; Y.-M. Chen et al. 2009; M. Pannella et al. 2009; P. Santini et al. 2009, 2017; G. E. Magdis et al. 2010; S. Oliver et al. 2010; A. Karim et al. 2011; G. Rodighiero et al. 2011; H. Shim et al. 2011; K.-S. Lee et al. 2012; N. Reddy et al. 2012; F. Salmi et al. 2012; K. E. Whitaker et al. 2012, 2014; H. J. Zahid et al. 2012; D. Kashino et al. 2013; J. Moustakas et al. 2013; D. Sobral et al. 2014; J. S. Speagle et al. 2014; C. L. Steinhardt et al. 2014; N. Lee et al. 2015; C. Schreiber et al. 2015; L. A. M. Tasca et al. 2015; I. Shivaei et al. 2015b; G. Erfanianfar et al. 2016; F. Belfiore et al. 2018; W. J. Pearson et al. 2018; P. Popesso et al. 2019a, b; S. K. Leslie et al. 2020; J. E. Thorne et al. 2021; J. Leja et al. 2022; P. Rinaldi et al. 2022; L. Sandles et al. 2022; W. M. Baker et al. 2023; P. Popesso et al. 2023; L. Clarke et al. 2024; J. W. Cole et al. 2025; P. Rinaldi et al. 2025; L. J. M. Davies et al. 2025a, b). Comparing SFMS measurements from the literature is non-trivial because of the use of different selection techniques and wavelengths (see e.g. A. Katsianis et al. 2016). Therefore, studies such as P. Popesso et al. (2023) and J. S. Speagle et al. (2014) have focused on converting all measurements to a common calibration, finding a consensus in the shape and normalization of the SFMS. Basically, there are three main factors that must be considered when studying the SFMS: (1) the estimation of the SFRs, obtained via dust-corrected emission line luminosities and/or SED fitting, (2) the sample selection, and (3) the stellar mass completeness of the sample. The latter is of utmost importance because the process of fitting the SFMS is highly sensitive to the mass range used (see Section 4.3). Thanks to surveys such as JADES, we are now able to construct large samples of galaxies complete in stellar mass up to $z \sim 9$.

The SFMS has been shown to evolve with redshift, both in observations (e.g. J. S. Speagle et al. 2014; P. Popesso et al. 2023) and simulations (e.g. S. Tacchella et al. 2016a; J. C. J. D'Silva et al. 2023; W. McClymont et al. 2025a). A convenient way to take this evolution into account when fitting the SFMS is to fit for the sSFR, adopting the following form:

$$\text{sSFR}_{\rm MS}(M_\star, z)[\text{Gyr}^{-1}] = s_{\rm b} \times \left(\frac{M_\star}{10^{10} M_\odot} \right)^\beta \times (1+z)^\mu, \quad (2)$$

as in S. Tacchella et al. (2016a). In this equation, the sSFR of the main sequence is determined by the redshift evolution (μ) of the SFMS, a stellar mass dependence (β, not to be confused with the UV continuum slope), and an overall normalization ($s_{\rm b}$, in units of Gyr^{-1}). We assume in this work no curvature of the SFMS masses at high stellar masses, since we focus on galaxies with stellar masses below 10^{11} M$_\odot$.

The same functional form as described by equation (2) can be used to describe the specific mass accretion rate (sMAR) of dark matter haloes. In this case, A. Dekel et al. (2013) show that $\mu_{\rm h}$ tends to 5/2 when a Lambda-cold dark matter (ΛCDM) cosmology in the Einstein–deSitter regime is adopted. The haloes mass dependence,
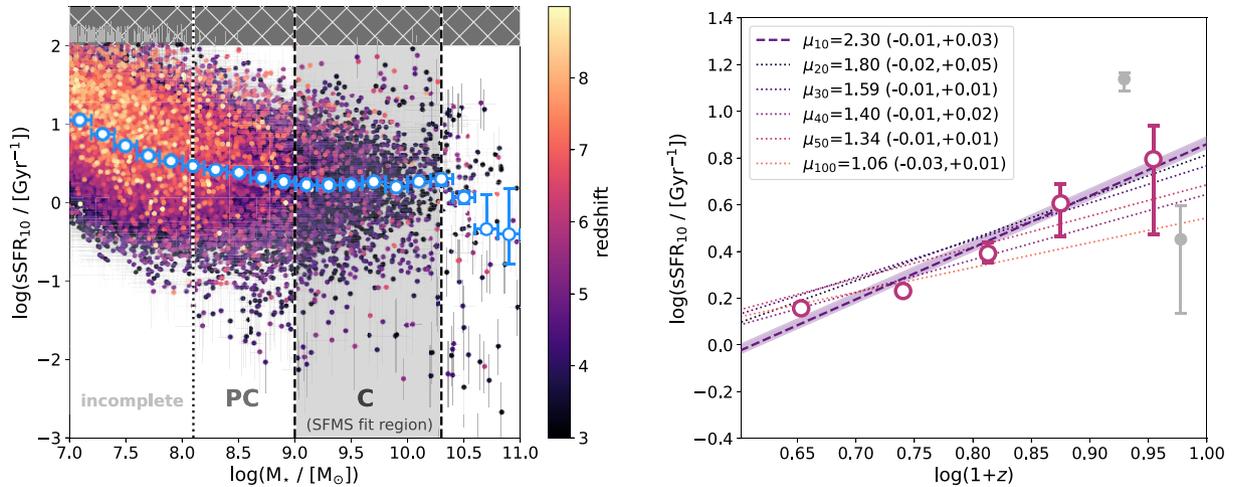
Figure 4. Stellar mass range and redshift evolution used to fit the SFMS. Left panel: specific star formation rate (sSFR$_{10}$) using the star formation averaged over the past 10 Myr (SFR$_{10}$), as a function of stellar mass for all galaxies in our sample with log($M_\star$/M$_\odot$) ≥ 7.0, colour-coded by redshift. The white circles with blue edges show the medians per stellar mass bins (0.2 width in logarithmic space). The vertical lines show different stellar mass completeness limits, delimiting three regions. The upper limit of the region labelled 'incomplete' is given by the mean stellar mass completeness estimated in Fig. 3 (log($M_\star$/M$_\odot$) ≈ 8.1). We note that the median sSFRs increase steadily below this limit. This trend is consistent with an increasing prevalence of rising SFHs at lower stellar masses, but it is also expected in biased samples that are incomplete in stellar mass. Interestingly, this behaviour continues (although less steeply) up to log($M_\star$/M$_\odot$) = 9.0, which we dub partially complete ('PC'). The shaded area shows galaxies with 9.0 ≤log($M_\star$/M$_\odot$) ≤ 10.3 (also shown as a blue hatched area in Fig. 3), we note that the sSFR flattens in this mass range, and thus we define this region as being complete ('C'), and use all galaxies in it to fit the SFMS (i.e. without imposing an SFR range). The upper limit of the complete region is motivated by the turnover of the SFMS at log($M_\star$/M$_\odot$) = 10.3. Finally, the hatched horizontal area shows the upper limit allowed given the time-scale used. Right panel: median sSFRs for galaxies with 9.0 ≤log($M_\star$/M$_\odot$) ≤ 9.5 as a function of redshift, the mass bin was selected because it is populated at all redshift bins. To increase numbers, we merge the two highest redshift bins (7 ≤ z ≤ 9). We fit a line to all medians to obtain the redshift evolution, μ_{10}, which we use as input when fitting the SFMS (see equation 2). The redshift evolution for all the remaining time-scales analysed in this work are shown as dotted lines.

β_h, is expected to contribute only in a minor way, with $\beta_h \approx 0.14$ (E. Neistein & A. Dekel 2008). The normalization of the sMAR, as measured from simulations, is $s_h = 0.03$ Gyr^{-1} (A. Dekel et al. 2013). While the sSFRs of SFMS galaxies do not need to track the sMAR of their haloes, the normalization of the SFMS has been shown to increase with lookback time as sSFR ∝ $(1 + z)^{\sim 2.2}$ (J. Brinchmann et al. 2004; E. Daddi et al. 2007; D. Elbaz et al. 2007; K. G. Noeske et al. 2007; K. E. Whitaker et al. 2012; J. S. Speagle et al. 2014; C. Schreiber et al. 2015; L. A. Boogaard et al. 2018; N. Caplar & S. Tacchella 2019; M. Donnari et al. 2019b; L. Sandles et al. 2022), which is very close to the expected value from the sMAR (N. Bouché et al. 2010; S. J. Lilly et al. 2013; S. Tacchella, M. Trenti & C. M. Carollo 2013; L. J. Tacconi et al. 2013; A. Rodríguez-Puebla et al. 2016; S. Tacchella et al. 2018).

In order to fit equation (2) to our data, we carefully selected the parameter space by following two steps, which are now briefly explained and are summarized in Fig. 4.

4.1 Mass range used in SFMS fitting

The slope of the SFMS is highly sensitive to the stellar mass range being used. This range should reflect the stellar mass completeness of the sample. In Section 3.2, we derive this limit following L. Pozzetti et al. (2010), and mention that it might be an underestimation of the stellar mass completeness if star formation is bursty, since it relies on a constant mass-to-light ratio. As a conservative approach, we decide to select the range of stellar mass we use in the SFMS by studying the behaviour of the sSFR as a function of stellar mass. In the left panel of Fig. 4, we show the relation between sSFR and stellar mass when using the shortest time-scale presented in this work, SFR$_{10}$

(comparable to SFRs derived with Hα). We find that the median sSFRs steadily decrease with stellar mass up to log($M_\star$/M$_\odot$) ∼ 8.1, in a region that we define as 'incomplete'. We note that the median sSFRs increase steadily below this limit. This trend is consistent with an increasing prevalence of rising SFHs at lower stellar masses, but it is also expected in biased samples that are incomplete in stellar mass. Since this trend becomes more pronounced with increasing incompleteness (e.g. at lower stellar masses) and is not reproduced in numerical simulations by increasing SFHs (W. Mc-Clymont et al. 2025a), we interpret it as primarily driven by sample incompleteness.

This behaviour continues up to log($M_\star$/M$_\odot$) = 9.0, albeit with a shallower slope, suggesting that this region still suffers from stellar mass completeness issues. This could be due to a combination of PROSPECTOR limitations when inferring SFRs at the lower mass end, of low-mass galaxies having preferentially increasing SFHs, and of SFHs being burstier than expected at this mass range, and is discussed further in Section 6.2. We dub this region as 'partially complete' ('PC'). Finally, we find that the sSFRs flatten at 9.0 ≤log($M_\star$/M$_\odot$) ≤ 10.3, where our upper mass limit agrees with the turnover observed by J. Leja et al. (2022; but see also N. Lee et al. 2015, where a turnover is observed at $M_\star$∼ 10^{10} M$_\odot$ at z < 1.3). We label this region as 'complete' ('C') and use it to fit the SFMS hereafter.

4.2 Redshift evolution used in SFMS fitting

In this work, we divide our sample into equally spaced redshift bins between z = 3 − 9, and note that as redshift increases, the number of galaxies decreases. As a result, if we fit equation (2) directly, leaving μ, β, and s_b as free parameters, our SFMS fits are dominated by the

Table 1. Best-fitting values to SFMS given in equation (2) for $9.0 \leq \log(M_\star/\mathrm{M}_\odot) \leq 10.3$ and $3 \leq z \leq 9$.

t_{average} [Myr]	s_b [Gyr^{-1}]	β	μ	$\eta(z=3)$ [Gyr^{-1}]	$\eta(z=9)$ [Gyr^{-1}]
10	$0.05^{+0.01}_{-0.01}$	$0.02^{+0.08}_{-0.06}$	$2.30^{+0.03}_{-0.01}$	$1.21^{+0.24}_{-0.24}$	$9.98^{+2.00}_{-2.00}$
20	$0.12^{+0.01}_{-0.01}$	$0.03^{+0.05}_{-0.06}$	$1.80^{+0.05}_{-0.02}$	$1.46^{+0.13}_{-0.12}$	$7.57^{+0.63}_{-0.63}$
30	$0.17^{+0.02}_{-0.01}$	$0.04^{+0.05}_{-0.05}$	$1.59^{+0.01}_{-0.09}$	$1.54^{+0.18}_{-0.09}$	$6.61^{+0.78}_{-0.39}$
40	$0.21^{+0.02}_{-0.02}$	$0.03^{+0.05}_{-0.04}$	$1.40^{+0.02}_{-0.01}$	$1.46^{+0.14}_{-0.14}$	$5.27^{+0.50}_{-0.50}$
50	$0.23^{+0.02}_{-0.02}$	$0.02^{+0.05}_{-0.05}$	$1.34^{+0.01}_{-0.01}$	$1.47^{+0.13}_{-0.13}$	$5.03^{+0.44}_{-0.44}$
100	$0.30^{+0.02}_{-0.02}$	$0.00^{+0.04}_{-0.04}$	$1.06^{+0.01}_{-0.03}$	$1.30^{+0.09}_{-0.09}$	$3.44^{+0.23}_{-0.23}$

Notes. Column 1: averaging time-scale of the SFR in units of Myr. Column 2: normalization in units of Gyr^{-1}. Column 3: stellar mass dependence. Column 4: redshift evolution. Columns 5 and 6: normalization of the SFMS, $\eta(z) = s_b(z) \times (1+z)^\mu$, at a fixed stellar mass of $\log(M_\star/\mathrm{M}_\odot)=10.0$, calculated at $z=3$ and 9, respectively.
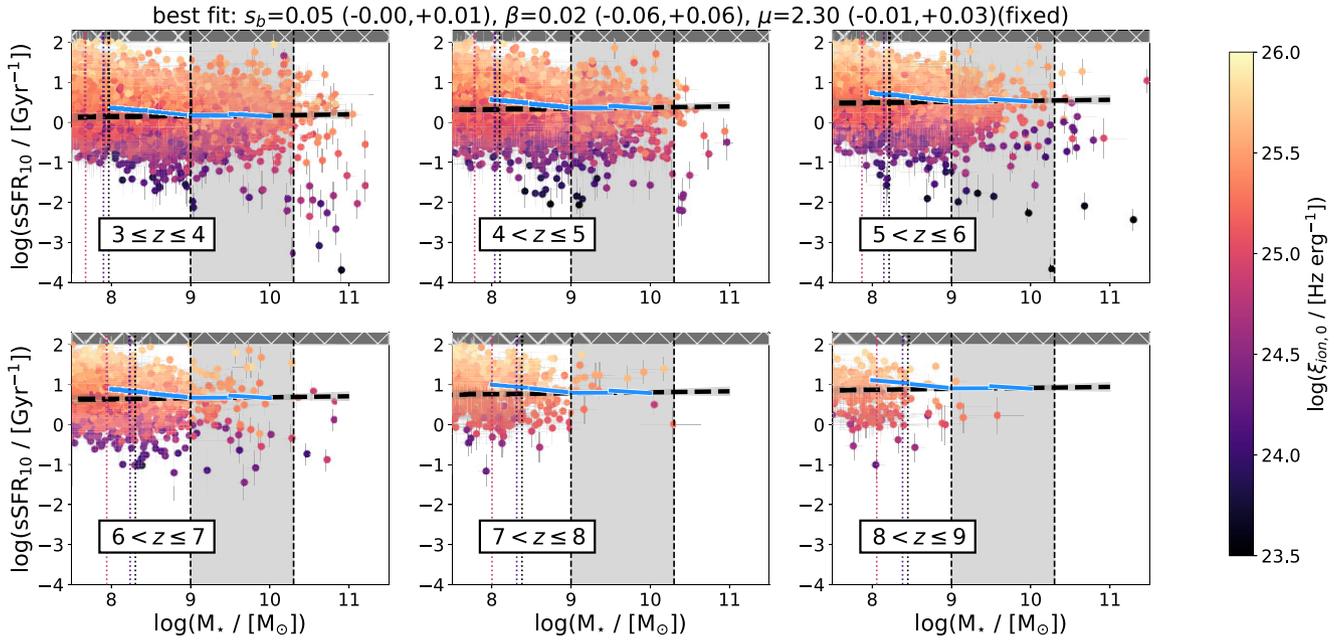
**Figure 5.** sSFR$_{10}$, as a function of stellar mass, colour-coded by their ionizing photon production efficiency ($\xi_{\mathrm{ion},0}$), and divided by redshift bins. The thick black dashed lines show the best fit to the SFMS given in equation (2), for galaxies with stellar masses in the range $9.0 \leq \log(M_\star/\mathrm{M}_\odot) \leq 10.3$ (indicated by the grey shaded region bounded by vertical dashed lines), and are extrapolated to all stellar masses in our sample. To improve the robustness of the fit at high redshift, the two highest redshift bins were grouped together when deriving the best-fitting relations, though they are shown separately in the figure for consistency with the redshift binning used throughout the paper. The blue filled lines show piecewise fits to the same equation in mass bins of stellar masses $\log(M_\star/\mathrm{M}_\odot) = 8.0$–$10.0$ in steps of 0.5 in logarithmic space. The grey hatched region shows the upper limit in sSFR, given by $\frac{1}{t_{\mathrm{average}}}$. For reference, we include the stellar mass completeness limits shown in Fig. 3: from left to right, the vertical dotted lines show the ultradeep, deep, and medium exposure times. We note that if we fit the SFMS using these limits instead ($\log(M_\star/\mathrm{M}_\odot) \gtrsim 8.1$), the slope of the fit becomes negative, as indicated by the discrepancy between the piecewise fit and the total fit in that stellar mass regime.

bulk of the galaxies at $z \leq 5$. Therefore, we constrain the redshift evolution of our sample separately (and for each SFR time-scale) and fix it as median and boundaries when fitting the SFMS. The right panel of Fig. 4 shows this exercise for SFR$_{10}$, where we have merged the two highest redshift bins ($7 \leq z \leq 9$), and fit a line in log space to the median sSFRs for galaxies with $9.0 \leq \log(M_\star/\mathrm{M}_\odot) \leq 9.5$, as a function of redshift. We choose to use this stellar mass bin since it contains galaxies at all redshifts here studied. For this averaging time-scale of 10 Myr, we find $\mu = 2.30^{+0.03}_{-0.01}$, a value that is similar to others found in the literature (e.g. L. Sandles et al. 2022; P. Popesso et al. 2023; W. McClymont et al. 2025a). We then extrapolate this redshift dependence of the SFMS to all stellar masses in our sample, and repeat this exercise with all the time-scales analysed in this work (shown as dotted lines and given in Table 1).

4.3 SFMS best-fitting parameters

Fig. 5 shows the results of fitting equation (2) to our data (see also Table 1), after following the previous steps, for SFRs averaged over the past 10 Myr and per redshift bin. The thick black dashed lines show the best fits to the SFMS (using galaxies in the 'complete' region, shown as a shaded grey area). For reference, we show the stellar mass completeness limits derived following L. Pozzetti et al. (2010) as vertical lines. To show how sensitive the SFMS fits are to the stellar mass limits, we show piecewise fits for stellar masses of $\log(M_\star/\mathrm{M}_\odot) = 8.0 - 10.0$ in logarithmic steps of 0.5 (blue filled lines). It can be seen that there is a discrepancy between the piecewise fits and the general fit at masses below $\log(M_\star/\mathrm{M}_\odot) = 9.0$, which is a result of this region being only partially complete in stellar mass. The individual points are colour-coded by their ionizing photon
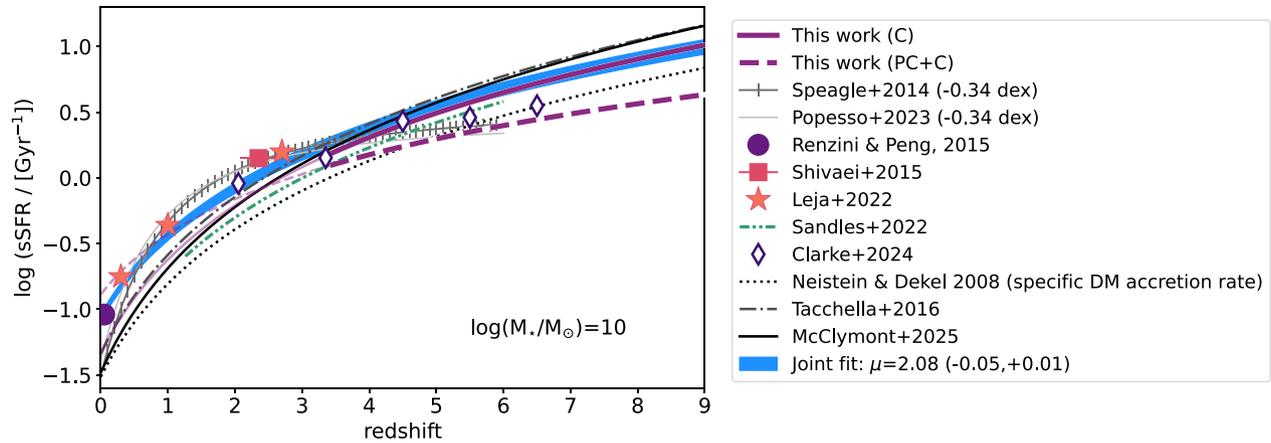
Figure 6. Comparison of the SFMS derived in this work to selected ones from the literature for recent star formation (either averaged over the past 10 Myr or derived from Hα fluxes). All markers and curves are shown for a fixed stellar mass of $10^{10} M_\odot$. The purple filled and dashed curves show the the SFMS fit to the complete ('C') and partially complete plus complete ('PC+C') samples, extrapolated to $z = 0$. The markers show the results for studies performed at redshift bins up to $z = 7$ (A. Renzini & Y.-j. Peng 2015; I. Shivaei et al. 2015b; J. Leja et al. 2022; L. Clarke et al. 2024,, as indicated in the legend). The grey curve shows the SFMS from P. Popesso et al. (2023), while the light grey line with vertical markers shows the J. S. Speagle et al. (2014) relation, both shifted by -0.34 dex to account for conversions in SFRs, as in A. E. Shapley et al. (2023). The green dash–dotted curve shows the parametrization provided by L. Sandles et al. (2022). The grey dash–dotted curve shows the results from S. Tacchella et al. (2016a), where only the normalization s_b was left as a free parameter, and the black filled line shows the SFMS based on the THESAN-ZOOM simulations from W. McClymont et al. (2025a). The discrepancies at $z < 3$ can be partially explained due to differences in how the stellar masses were inferred, and how complete the samples are in stellar mass, but mainly arise due to the sample selections and conversions of Hα luminosities to SFRs. The black dotted curve shows the expected specific mass accretion ratio of dark matter haloes from E. Neistein & A. Dekel (2008), using the $M_\star$–M_{halo} conversion from S. Tacchella et al. (2018). It is important to note that using a different conversion would result in slightly shifting this curve, but that the redshift evolution of the SFMS found in this work is remarkably similar to the specific mass accretion ratio of dark matter haloes. Finally, a joint fit to the shifted J. S. Speagle et al. (2014) up to $z = 3$ with our fit to the complete sample ($z = 3 - 9$) is shown as a blue shaded area. Including the lower redshift results from literature in the fit results in a slightly shallower evolution with redshift ($\mu \approx 2.08$ instead of 2.30).

production efficiency assuming an escape fraction of zero, $\xi_{ion,0}$, estimated by PROSPECTOR (see e.g. C. Simmonds et al. 2023, 2024a). This quantity is essentially the ratio between recent (averaged over the past 10 Myr) star formation, and the one sustained over the past 100 Myr (C. Simmonds et al. 2024a). Although this ratio directly probes the recent SFH, its variance for an ensemble of galaxies measures short-term star formation variability (N. Caplar & S. Tacchella 2019). As expected, the distance to the SFMS is related to $\xi_{ion,0}$, where the galaxies that are most efficient producers of ionizing radiation lie above the relation.

4.4 The normalization of the SFMS

The best-fitting parameters for all adopted SFR averaging time-scales are listed in Table 1. We find that the normalization s_b increases with averaging time-scale, while the redshift dependence μ decreases with averaging time-scale. While s_b quantifies the normalization of the SFMS at a given redshift as per equation (2), we must also account for the explicit redshift evolution through the $(1 + z)$-term (and given by μ) to compare absolute normalization values across time-scales (see Figs 4 and 6). At $z = 3$ and $\log(M_\star/M_\odot) = 10$, we measure an SFMS normalization, which we define as $\eta(z) = s_b(z) \times (1 + z)^\mu$, of 1.2 Gyr^{-1} for $t_{average} = 10$ Myr and 1.5 Gyr^{-1} for $t_{average} = 50$ Myr. At $z = 9$, we find an SFMS normalization of 10.0 Gyr^{-1} for $t_{average} = 10$ Myr and 5.0 Gyr^{-1} for $t_{average} = 50$ Myr (see Table 1). The interpretation of this trend is not straightforward, as it reflects the interplay of two competing effects: bursty star formation and the overall rise of SFHs. As shown by N. Caplar & S. Tacchella (2019, see also M. Donnari et al. 2019a; K. G. Iyer et al. 2020), the SFMS normalization depends on both the stochasticity of star formation and the averaging time-scale of the SFR measurement. Short-time-scale indicators capture rapid fluctuations, including low-

SFR episodes, whereas long-time-scale indicators smooth over these variations, leading to higher inferred average SFRs and an elevated normalization. An effective tool to understand the power contained in SFR fluctuations at a specific time-scale is the power spectral density (PSD). On short time-scales (< 10 Myr), galaxy growth is governed by internal processes such as Giant Molecular Cloud (GMC) formation, star formation, and stellar feedback (C. Leitherer et al. 1999; J. C. Tan 2000; E. J. Tasker 2011; C.-A. Faucher-Giguère 2018; S. M. Benincasa et al. 2020). On intermediate time-scales (< 100 Myr), large-scale feedback and gas cycling dominate (V. A. Semenov, A. V. Kravtsov & N. Y. Gnedin 2017; E.-j. Shin et al. 2023), while on longer time-scales, external drivers such as mergers become important (B. Robertson et al. 2006; D. Puskás et al. 2025). Crucially, the dependence of SFMS normalization on the averaging time-scale, $t_{average}$, encodes information about the stochastic nature of galaxy SFHs, e.g. its PSD (N. Caplar & S. Tacchella 2019). The higher SFMS normalization on the 50 Myr relative to the 10 Myr averaging time-scale at $z = 3$ is consistent with a break time-scale of $\tau_{break} \approx 50$ Myr and a PSD slope $\alpha = 2$, in agreement with the expectations of bursty star formation and the predictions of N. Caplar & S. Tacchella (2019, see their fig. 5). However, towards higher redshifts, the trend reverts and the normalization is higher for shorter averaging time-scales.

A second factor affecting the interpretation of the SFMS normalization is the presence of rising SFHs. For galaxies with rising SFHs, the SFR averaged over shorter time-scales is systematically higher than when averaged over longer time-scales. Consequently, if most galaxies follow rising SFHs, the SFMS normalization is expected to be higher when measured on short time-scales. We expect, in particular towards higher redshift, the fraction of galaxies with increasing SFHs to increase (e.g. S. Tacchella et al. 2018). Indeed, for galaxies in our sample with $8.1 \lesssim \log(M_\star/M_\odot) \leq 10.3$, the fraction
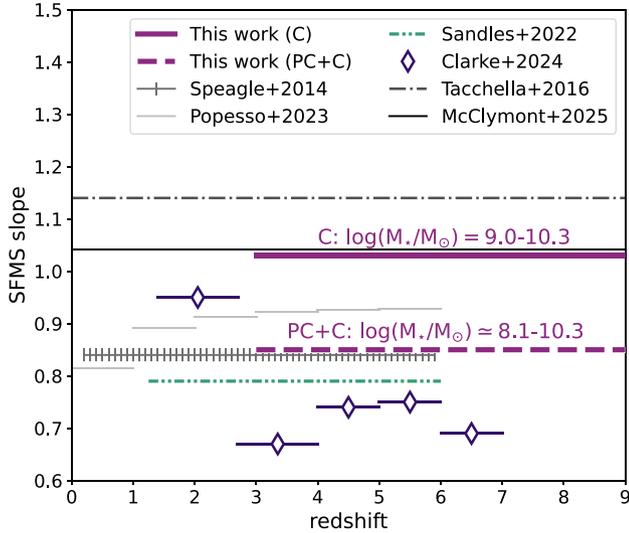
Figure 7. Comparison of the SFMS slope, defined as the slope of the logarithmic relation between SFR_{10} and stellar mass ($SFR \propto M_\star^\alpha$, where $\alpha = 1 + \beta$ with β from equation 2), as a function of redshift for a selection of works shown in Fig. 6. As can be seen, the slope when considering the complete ('C') sample approaches 1, while for the partially complete plus complete sample ('PC+C') the slope is shallower. This discrepancy is potentially driven by stellar mass completeness.

of galaxies with $SFR_{10}/SFR_{100} > 2$ increases from 0.31 to 0.55, from $z = 3$ to 9. The elevated SFMS normalization measured on shorter time-scales at $z > 6$ is therefore primarily driven by the prevalence of rising SFHs in early galaxies. While this complicates the use of normalization alone as a diagnostic of star formation variability, the scatter around the SFMS provides a more direct probe of burstiness (see Section 5.1). In future work (Bevins et al. (in preparation)), we will build on this analysis by forward modelling the scatter as a function of $t_{average}$, enabling tighter constraints on the PSD and the temporal coherence of star formation in the high-redshift Universe.

4.5 Comparison of our SFMS to literature

We now compare our obtained SFMS (equation 2 and Table 1, using $sSFR_{10}$) with other studies in the literature, both at the same redshift and lower redshifts. In the comparison, we focus on the normalization of the SFMS (Fig. 6) and the slope that describes the stellar mass dependence (Fig. 7). Specifically, we compare our SFMS to $z < 7$ studies by A. Renzini & Y.-j. Peng (2015), I. Shivaei et al. (2015b), J. Leja et al. (2022), L. Sandles et al. (2022), and L. Clarke et al. (2024), as well as the results from J. S. Speagle et al. (2014) and P. Popesso et al. (2023), which are both based on compilations of SFR measurements[3] up to $z = 6$. A. Renzini & Y.-j. Peng (2015) and I. Shivaei et al. (2015b) derived SFRs from Hα luminosities using Balmer decrement-based dust corrections for local SDSS galaxies and Multi-Object Spectrometer for Infrared Exploration (MOSFIRE) observations for galaxies at $z \sim 2$, respectively. J. Leja et al. (2022) derived their SFMS from SED fitting with the PROSPECTOR code, focusing on galaxies at $0.5 < z < 3$, while L. Sandles et al. (2022) used SED fitting with BEAGLE (J. Chevallard & S. Charlot 2016) to derive the SFMS at $1.25 < z < 6$. Finally, we include the recent

[3] Both the J. S. Speagle et al. (2014) and the P. Popesso et al. (2023) relations have been shifted by a factor of -0.34 dex, as suggested by A. E. Shapley et al. (2023), to account for SFR conversions.

measurements by L. Clarke et al. (2024), based on ~ 150 galaxies at $1.4 < z \le 7$, who used Balmer line luminosity, SED fitting, and UV luminosity to derive SFRs.

Fig. 6 compares the normalization of the SFMS from this work using $sSFR_{10}$ at fixed stellar mass of $\log(M_\star/M_\odot) = 10.0$ (for both the 'complete' and 'complete+partially complete' samples, extrapolated to $z = 0$) to other selected results from the literature. We provide an updated SFMS prescription (indicated with the thick blue line) from $z = 0$ to 9, which slightly flattens the redshift evolution, particularly at $z > 3$ (with $\mu \approx 2.08$). We find overall good agreement between our and the literature values, with offsets of less than 0.3 dex, which can be attributed to varying stellar mass and SFR measurement methods. In particular, L. Sandles et al. (2022) find a redshift evolution of $\mu = 2.40 \pm 0.18$, which is consistent with our work. We also compare our results to simulations by W. McClymont et al. (2025a) and S. Tacchella et al. (2016a), and find that our SFMS matches the predictions from these models. Moreover, we find that the normalization of the SFMS follows the specific dark matter accretion rate from E. Neistein & A. Dekel (2008; see also S. J. Lilly et al. 2013), in agreement with the conclusions from L. Sandles et al. (2022).

Fig. 7 shows the slope of the SFMS as a function of redshift from our work and estimates from the literature. We define SFMS slope as the slope of the logarithmic relation between SFR_{10} and stellar mass (e.g. $SFR \propto M_\star^\alpha$, where $\alpha = 1 + \beta$ with β from equation 2). Since the SFMS slope is significantly more affected by sample selection and completeness than the SFMS normalization, it is not surprising that we find a larger scatter in values from the literature. Specifically, we note that many observational studies derive a slope to the $M_\star$–SFR relation that is less than 1 (e.g. $\alpha \approx 0.7 - 0.9$; J. S. Speagle et al. 2014; L. Sandles et al. 2022; P. Popesso et al. 2023; L. Clarke et al. 2024), which would be negative in $M_\star$–sSFR (e.g. $\beta < 0$). We define our conservative completeness cut based on where the slope in $M_\star$–sSFR starts to become negative. Indeed, mass incompleteness leads to a shallower derived slope of $M_\star$–SFR: discrepancies in the SFMS shape at $z < 6$ can be explained by stellar mass incompleteness and sample biases, with lower mass galaxies being under-represented (as demonstrated in W. McClymont et al. 2025a). We demonstrate the difference in the derived slopes if we push to $10^8 M_\odot$ into the 'partially complete' regime, which yields a slope of 0.85 (compared to 1.03 in the complete regime).

5 SCATTER OF THE SFMS

Beyond the average relation between SFR and stellar mass, the scatter around the SFMS encodes valuable information about the diversity of galaxy growth histories and the stochasticity of mass assembly across cosmic time. Previous studies have found intrinsic scatter values that slightly vary with redshift and stellar mass, with $\sigma_{int} \le 0.5$ dex (P. S. Behroozi, R. H. Wechsler & C. Conroy 2013; P. Kurczynski et al. 2016; L. Sandles et al. 2022), while others report little-to-no dependence on stellar mass ($\sigma_{int} \sim 0.2 - 0.3$ dex; D. Elbaz et al. 2007; K. G. Noeske et al. 2007; C. Schreiber et al. 2015). We stress that these studies mostly focused on massive galaxies, above $10^9 M_\odot$. Burstiness of star formation tends to be associated with low stellar masses (D. R. Weisz et al. 2012; K. Guo et al. 2015) due to the relative importance of stellar feedback (G. S. Stinson et al. 2007; T. Dome et al. 2024). In low-mass galaxies, this has been attributed to shallow gravitational potentials being unable to retain their ISM after the onset of stellar (e.g. SNe) feedback (P. F. Hopkins et al. 2023), as well as to the inherently stochastic nature of star formation driven by the finite lifetimes of GMCs and their discrete sampling (S. Tacchella
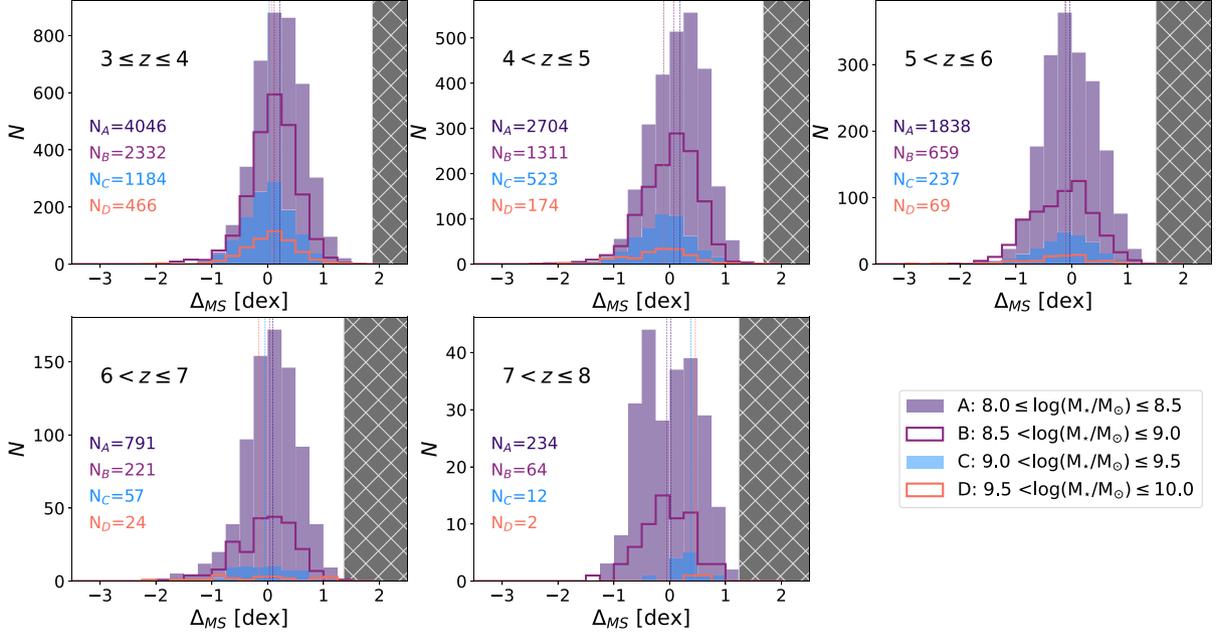
Figure 8. Histograms showing the distance to the SFMS, Δ_{MS}, using the star formation averaged in the past 10 Myr (shown as thick black dashed lines in Fig. 5), as function of redshift bin up to $z = 8$. We define four stellar mass bins, at $\log(M_\star/\mathrm{M}_\odot) = 8.0$–$10.0$, as indicated in the legend. For each panel, the number of galaxies in each mass bin is shown, as well as the median of each distribution. The grey hatched region shows the maximum permitted Δ_{MS} at each redshift, for $\log(M_\star/\mathrm{M}_\odot) = 8.0$. Although composed of very few galaxies (< 100 in total), the histograms tend to have a tail towards the lower values and thus cannot be described appropriately by a Gaussian distribution.
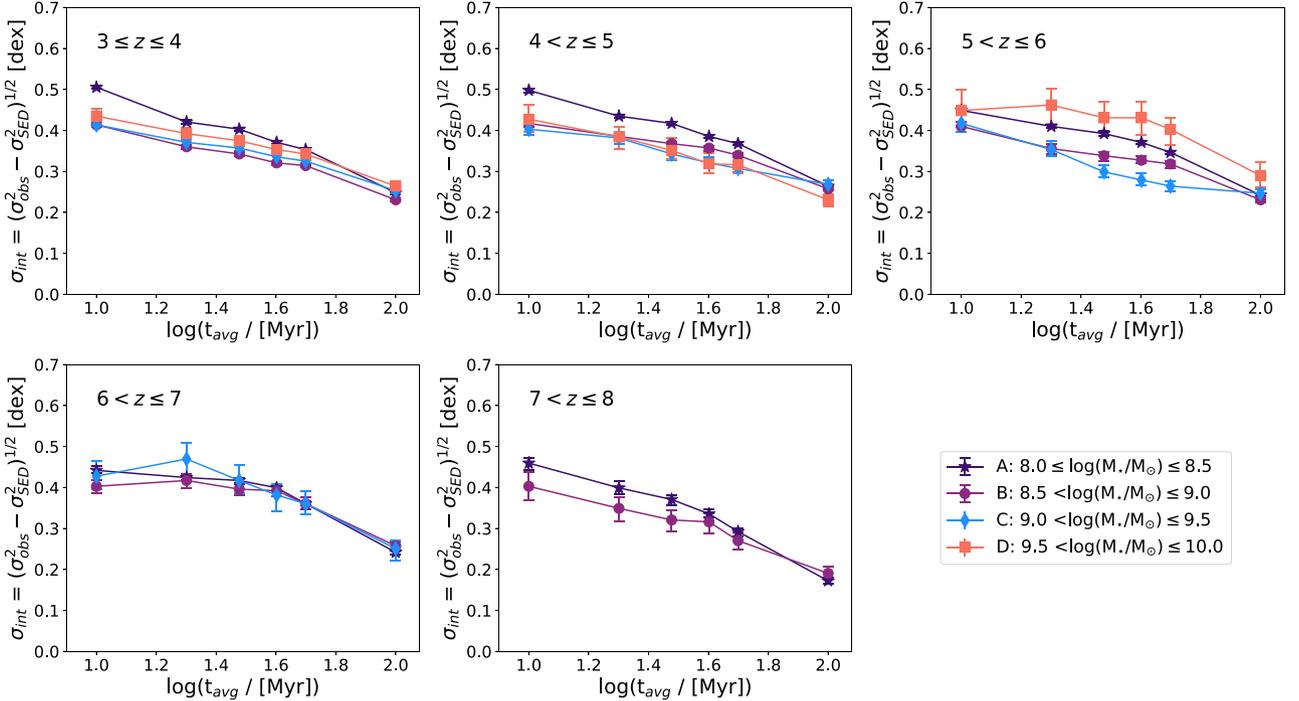
Figure 9. Intrinsic scatter of the SFMS, σ_{int}, as a function of redshift and stellar mass, as indicated in the legend, where $\sigma_{\mathrm{int}} = \sqrt{\sigma_{\mathrm{obs}}^2 - \sigma_{\mathrm{SED}}^2}$. Only bins with at least 30 galaxies are shown. The intrinsic scatter decreases as averaging time-scales increase for every mass and redshift bin studied, from $\sigma_{\mathrm{int}} \approx 0.4 - 0.5$ at 10 Myr down to $\sigma_{\mathrm{int}} \approx 0.2$ at 100 Myr. This behaviour is expected when star formation is bursty, as averaging over longer time-scales smooths out episodic bursts and (mini-)quenching events, reducing the scatter in the SFRs.

et al. 2020). The increase of burstiness with redshift has been attributed to increasingly stochastic IGM inflow (W. McClymont et al. 2025a), but also may be due to the shorter dynamical time-scales of high-redshift galaxies (C.-A. Faucher-Giguère 2018; S. Tacchella et al. 2020). In support of the relation between bursty star formation and scatter of the SFMS, several works have found the
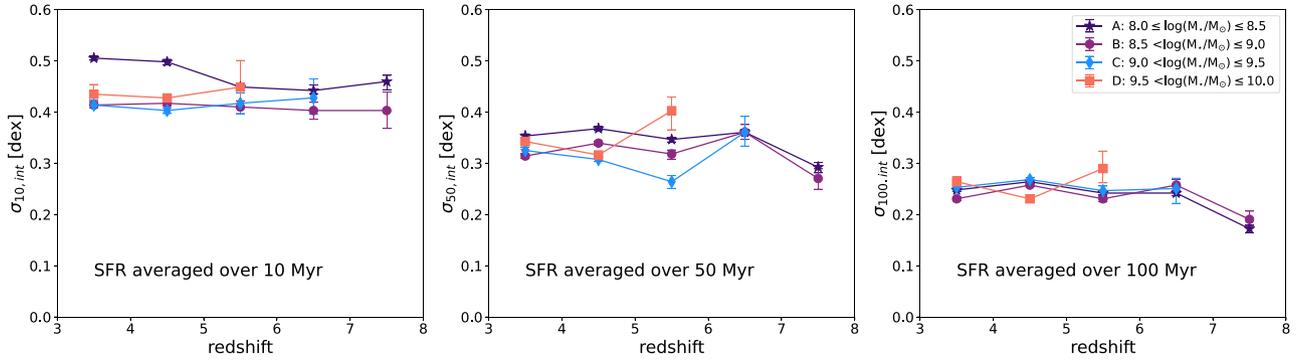
Figure 10. Intrinsic scatter of the SFMS, σ_{int}, as a function of redshift, for three selected averaging time-scales, from left to right: 10, 50, and 100 Myr. Only bins containing at least 30 galaxies are shown. As expected, σ_{int} decreases as time-scales increase. Interestingly, we observe no strong dependence of σ_{int} on redshift.

scatter to be higher for low-mass galaxies, both in observations (G. Kauffmann 2014; D. R. Weisz et al. 2014; P. Santini et al. 2017; L. A. Boogaard et al. 2018; H. Atek et al. 2022; Y. Asada et al. 2024; J. W. Cole et al. 2025) and simulations (S. Shen et al. 2014; A. Domínguez et al. 2015; K. G. Iyer et al. 2020; W. McClymont et al. 2025a). We note that this mass dependence is not always observed. For example, P. Kurczynski et al. (2016), focusing on $z \sim 0.5 - 3$, do not find a significant dependence of the intrinsic scatter on stellar mass. However, they cannot rule out this behaviour since the smallest averaging time-scale they study is ~ 100 Myr, which would smooth out bursty star formation on shorter time-scales. Interestingly, some studies argue for an increase of the scatter as a function of stellar mass for galaxies with $\log(M_\star/M_\odot) = 10.0 - 11.5$ (K. Guo, X. Z. Zheng & H. Fu 2013; P. Popesso et al. 2019a, b; S. Sherman et al. 2021; J. W. Cole et al. 2025), but we caution that low-number statistics and that quenching of star formation in massive galaxies could contribute to boosting the scatter (K. E. Whitaker et al. 2014; N. Lee et al. 2015; A. R. Tomczak et al. 2016; W. M. Baker et al. 2025b). This mass range is outside of the scope of this work, since we do not have the statistics to study this stellar mass bin at all redshifts.

5.1 Estimating the scatter of the SFMS

To estimate the scatter of the SFMS as a function of redshift and stellar mass, we define four stellar mass bins as follows:

  (i) A: $8.0 \leq \log(M_\star/M_\odot) \leq 8.5$.
  (ii) B: $8.5 < \log(M_\star/M_\odot) \leq 9.0$.
  (iii) C: $9.0 < \log(M_\star/M_\odot) \leq 9.5$.
  (iv) D: $9.5 < \log(M_\star/M_\odot) \leq 10.0$.

Since we do not have any galaxies in bin D at $z > 8$, we only focus on redshift bins up to $z = 8$. We calculate the logarithmic distance to the SFMS fits, Δ_{MS}, for each time-scale (given by inserting the best-fitting parameters in Table 1 into equation 2), as a function of redshift and stellar mass bins. The resulting histograms for sSFR$_{10}$ are shown in Fig. 8, where the hatched grey area shows the time-scale-dependent maximum SFR limit (SFR$_{max} = M_\star/t_{average}$). The number of galaxies in each stellar mass bin is shown per redshift bin. As can be seen, the distributions tend to have a tail towards lower Δ_{MS} values. Moreover, we are likely missing galaxies in this region (R. Feldmann 2017). Although the number of galaxies that compose these tails is small (< 100 galaxies in total), they have the effect of making the distributions non-Gaussian. Therefore, in order to obtain the observed scatter of the SFMS, we mirror these distributions around zero (which has been shown to be a good estimation by

W. McClymont et al. 2025a) and define the observed scatter, σ_{obs}, as the standard deviation of the now Gaussian distributions (see Appendix B).

After obtaining σ_{obs}, we estimate the intrinsic scatter, σ_{int}, by subtracting the uncertainties on stellar mass and SFR from SED modelling in quadrature, and obtain errors by bootstrapping the distributions 100 times each. The SED errors, which are obtained by averaging the uncertainties inferred by PROSPECTOR per stellar mass and redshift bin, vary between $\approx 0.1 - 0.3$ dex: they decrease as a function of averaging time-scale and increase as a function of redshift. We note that these errors do not account for systematics such as outshining. In Fig. 9, we show the intrinsic scatter obtained after following the steps described above, for bins where we have at least 30 galaxies. As expected, the intrinsic scatter decreases as a function of averaging time-scale from $\sigma_{int} \approx 0.4 - 0.5$ at 10 Myr to $\sigma_{int} \approx 0.2$ at 100 Myr, for all bins studied, with slight variations depending on the stellar mass analysed, in agreement with previous studies (e.g. D. Elbaz et al. 2007; J. W. Cole et al. 2025). Fig. 10 shows σ_{int} for three different lookback times as a function of redshift, from left to right: 10, 50, and 100 Myr for bins containing at least 30 galaxies. As expected, the scatter decreases as the averaging time-scales increase, from ~ 0.4 to ~ 0.2. Our measurements provide a robust constraints on the intrinsic scatter of the SFMS across a wide stellar mass range at $z = 3 - 8$, based on homogeneous, high-quality photometry. We find no strong trend in the scatter with redshift, indicating a relatively stable level of variability in star formation over this epoch. However, we do observe a weak mass dependence, with slightly larger scatter at lower stellar masses at shorter time-scales. These findings are broadly consistent with theoretical expectations (e.g. W. McClymont et al. 2025a).

5.2 Constraint on star formation burstiness

We estimate short-term burstiness, σ_{ST}, by measuring the difference in the intrinsic scatter of the SFMS between averaging time-scales of 10 and 50 Myr, thereby isolating the contribution from rapid, short-term processes on time-scales of 10 Myr to the ones on time-scales of 50 Myr:

$$\sigma_{ST} = \sqrt{\sigma_{10,int}^2 - \sigma_{50,int}^2}, \qquad (3)$$

as in W. McClymont et al. (2025a).

Fig. 11 shows the short-term burstiness, σ_{ST}, as a function of redshift for the four stellar mass bins defined above. This quantity represents the first robust measurement of burstiness imprinted onto
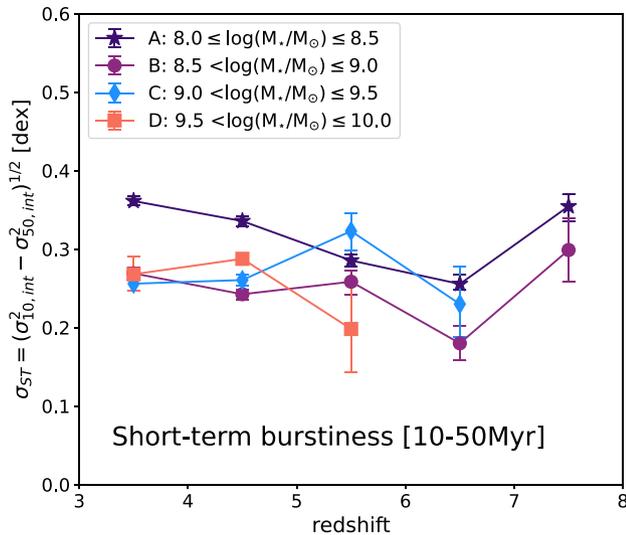
Figure 11. Short-term burstiness, σ_{ST}, defined as the difference between the intrinsic scatter of the SFMS between a lookback time of 10 and 50 Myr, as a function of redshift. Our findings suggest SFHs are bursty for all of the stellar mass bins here considered. We draw attention to the lowest mass bin ('A'), which contains the largest amount of galaxies, and has indications of being slightly burstier. In this mass bin, we see that σ_{ST} decreases between $z = 3$ and 6, and increases at $z > 7$. This can be interpreted as an indication of two different mechanisms dominating the short-term scatter of the SFMS: environmental effects at $z > 8$, and internal processes at $z < 8$. We note that the trends persist if we look at the difference between lookback times of 10 and 100 Myr instead.

SFMS scatter, specifically isolating the contribution from rapid fluctuations in star formation. We find that $\sigma_{\mathrm{ST}} \approx 0.2 - 0.4$ dex across all redshifts and mass bins, indicating that short-term variability is a significant and persistent feature of galaxy growth during EoR ($z = 3 - 8$). While there is no strong trend with stellar mass, we observe that the lowest mass bin ($8.0 \leq \log(M_\star/M_\odot) \leq 8.5$) shows systematically higher short-term burstiness, with a dip at $z = 6 - 7$. The significance and origin of this feature remain uncertain due to observational limitations, and we caution that its interpretation is speculative.

Interestingly, a similar dip in σ_{ST} at $z \sim 6 - 7$ has been reported in the THESAN-ZOOM simulations (W. McClymont et al. 2025a), where it arises despite a decrease in the overall scatter $\sigma_{\mathrm{int},10}$ with redshift. Thanks to the ability to disentangle different sources of variability, these simulations show that short-term burstiness is primarily driven by internal processes (e.g. feedback, stochastic star formation), but that externally driven variability – particularly fluctuations in inflow from the circumgalactic medium – becomes increasingly important at higher redshift. This supports the interpretation that while internal processes dominate short-term variability, the slight increase in σ_{ST} at early times may reflect more rapid and stochastic gas accretion in the early Universe.

5.3 Investigating the long-term variability of the SFMS

In the previous analysis of the SFMS scatter, we have assumed that individual galaxies evolve about the same SFMS and the scatter is mainly caused by fluctuations on time-scales of tens of Myr. We now look into whether galaxies evolve about the SFMS on even longer time-scales (e.g. 100s of Myr), which basically would imply that

galaxies do not evolve around a single SFMS (S. G. Patel et al. 2009; M. D. Gladders et al. 2013; D. D. Kelson 2014; L. E. Abramson et al. 2016; A. Paulino-Afonso et al. 2020; E. Wang & S. J. Lilly 2020). In order to assess this, we follow L. E. Abramson et al. (2016), and J. T. Wan et al. (2024, 2025) and plot the inferred stellar age, as measured by the half-mass assembly time, t_{50}, as a function of the distance of the SFMS, Δ_{MS}, in Fig. 12.

The left panel of Fig. 12 shows the relation between t_{50} and Δ_{MS} for individual galaxies in our sample, with colours indicating different stellar mass bins. Before interpreting these trends, we caution that t_{50} is a particularly challenging quantity to constrain. This is especially true for galaxies with rising SFHs, where the light from younger stellar populations can outshine the contribution of older stars (C. Papovich et al. 2023; S. Tacchella et al. 2023; R. Endsley et al. 2024; D. Narayanan et al. 2024; C. Witten et al. 2025), leading to large uncertainties in the inferred stellar ages.

We identify two tentative trends in the $t_{50} - \Delta_{\mathrm{MS}}$ plane. First, t_{50} appears to be anticorrelated with Δ_{MS}, such that, on average, galaxies lying above the SFMS tend to be younger. Similar behaviour has been reported in previous studies (e.g. D. Langeroodi & J. Hjorth 2024; P. Rinaldi et al. 2025; J. T. Wan et al. 2025). However, this correlation is very weak, as indicated by the best-fit relation shown in the right panel of Fig. 12. For galaxies with $\log(M_\star/M_\odot) > 8.0$, the median stellar age changes by less than a factor of two when moving from 1 dex below to 1 dex above the SFMS. The trend becomes significant only for the lowest mass galaxies, where the age differences are more pronounced, but note that the steepness of the lower mass bin is potentially due to stellar mass incompleteness.

Secondly, when dividing our sample into stellar mass bins, we find that more massive galaxies tend to have older stellar populations. The median ages of each mass bin, shown in Fig. 12, further support the conclusion that higher mass galaxies are typically older. In addition, the fraction of galaxies with low Δ_{MS} increases with stellar mass, consistent with a larger proportion of massive systems undergoing quenching.

In summary, we find a broadly consistent picture in which younger galaxies tend, on average, to lie above the SFMS, likely reflecting the impact of recent starburst episodes in these systems. However, the overall correlation between stellar age and SFMS offset is weak, suggesting that short-term fluctuations in star formation dominate over longer term evolutionary trends.

6 CONSEQUENCES OF BURSTY STAR FORMATION ACROSS COSMIC TIME

We have shown that the SFMS can be parametrized up to $z = 9$, and that SFHs are in general bursty across cosmic time. In this section, we explore the consequences and implications of this result on three key points: (1) the observed overabundance of UV-bright galaxies at $z > 10$, (2) the considerations that should be taken into account when estimating the mass completeness limits of samples, and (3) the connection between bursty star formation and the reionization of the Universe.

6.1 Implications at $z > 10$

Since the launch of the *JWST*, several galaxies have been observed at $z > 10$ (M. Castellano et al. 2022; R. P. Naidu et al. 2022; E. Curtis-Lake et al. 2023; C. T. Donnan et al. 2023; S. L. Finkelstein et al. 2023; Y. Harikane et al. 2023; B. E. Robertson et al. 2023; C. M. Casey et al. 2024; F. D'Eugenio et al. 2024; K. N. Hainline
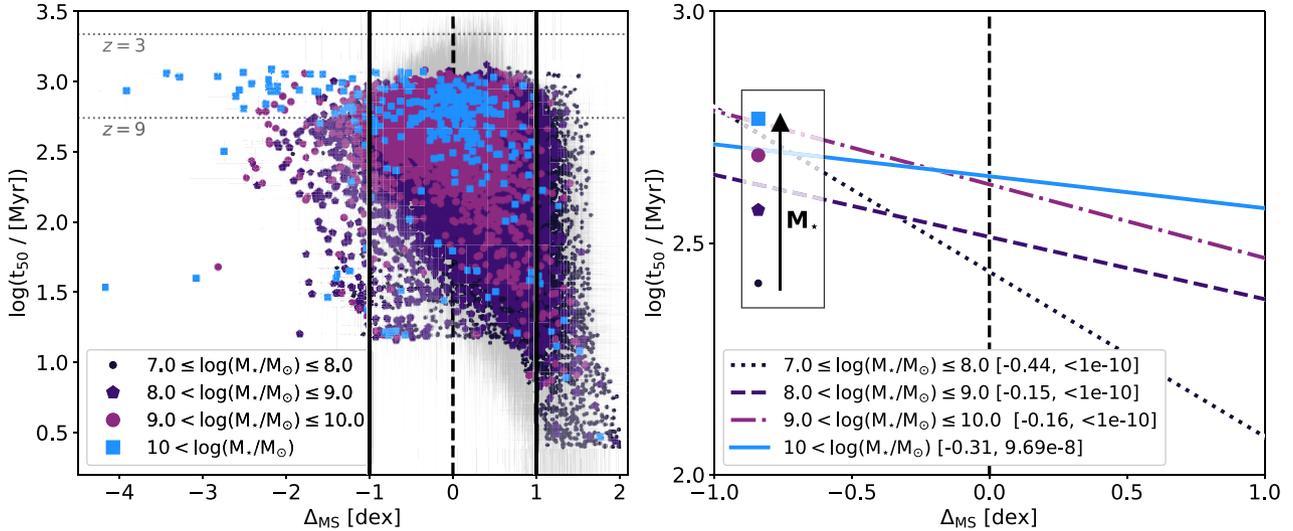
Figure 12. Relation between stellar age (e.g. half-mass assembly time, t_{50}) and distance from the SFMS, Δ_{MS}, using sSFR$_{10}$. Left panel: scatter plots for different stellar mass bins, as indicated in the legend. The lower cut-off in t_{50} is due to the minimum lookback time in the SFH (5 Myr). The vertical dashed line shows $\Delta_{MS} = 0$, while the vertical filled lines delimit the region where $-1 \leq \Delta_{MS} \leq 1$. The horizontal dotted lines show the age of the Universe at $z = 3$ and 9. There are two tentative trends that arise in this figure. First, a relation between the position of the galaxies on the SFMS and their age, suggesting that (on average) younger galaxies lie above the SFMS. Secondly, as stellar mass increases, galaxies are typically older and can reach lower Δ_{MS} values (possibly due to quenching). Right panel: best-fitting lines to each stellar mass bin considered, for galaxies within the vertical filled black lines in the left panel, to illustrate the trend between age, stellar mass, and Δ_{MS}. For each stellar mass bin, we provide in brackets the Spearman's rank coefficients in the format [correlation, *p*-value]. For reference, the correlation coefficient can adopt values between -1 and 1, where 0 represents no association between parameters, and a *p*-value close to zero indicates that the correlation – even if weak – is unlikely to be due to chance. We note that the steepness of the slope for galaxies with $\log(M_\star/M_\odot) = 7.0 - 8.0$ is potentially due to stellar mass incompleteness in that bin. Finally, the markers show the median t_{50} value per mass bin, confirming that, on average, galaxies become more massive as they age. Importantly, the overall correlation between stellar age and SFMS offset is weak, as indicated by the Spearman's rank coefficients, suggesting that short-term fluctuations in star formation dominate over longer term evolutionary trends.

et al. 2024; Y. Harikane et al. 2024; D. J. McLeod et al. 2024; B. Wang et al. 2024; V. Kokorev et al. 2025; R. P. Naidu et al. 2025; J. M. Helton et al. 2025b). These observations have challenged our understanding of galaxy evolution, since measurements of the UV luminosity function (e.g. S. L. Finkelstein et al. 2023; N. J. Adams et al. 2024; C. T. Donnan et al. 2024; B. Robertson et al. 2024; L. Whitler et al. 2025) have revealed a potential overabundance of UV-bright galaxies in the early Universe, when compared to model predictions. Some ways to reconcile theory with observations are to invoke significantly increased burstiness in galaxies at $z > 9$, high star formation efficiencies and suppressed feedback in these galaxies (A. Dekel et al. 2023; Z. Li et al. 2024), low dust attenuation as redshift increases (A. Ferrara, A. Pallottini & P. Dayal 2023), AGN activity (which has been detected at $z > 10$, see e.g, R. Maiolino et al. 2024; J. Scholtz et al. 2024), or a top-heavy IMF (A. Trinca et al. 2024; V. Mauerhofer et al. 2025). Our focus here is variations in SFRs that arise from bursty SFHs can lead to strong UV variability which could, in turn, explain the observed overabundance of UV-bright galaxies at $z > 10$. In brief, high-redshift galaxies could be upscattered due to a recent burst in star formation, making them bright enough to dominate the bright end of the UV luminosity function (K. Ren, M. Trenti & C. A. Mason 2019; C. A. Mason, M. Trenti & T. Treu 2023; J. Mirocha & S. R. Furlanetto 2023; J. B. Muñoz et al. 2023; X. Shen et al. 2023).

At $z < 9$, galaxies have SFHs that are *consistent* with being bursty (e.g. R. Endsley et al. 2023; Y. Asada et al. 2024; C. Simmonds et al. 2024a; T. J. Looser et al. 2025; J. W. Cole et al. 2025; W. M. Baker et al. 2025a). In this work, we explicitly demonstrate that galaxies at $z = 3 - 9$ exhibit bursty SFHs, as evidenced by excess star formation variability on 10 Myr time-scales compared

to 50 Myr. Furthermore, we provide a quantitative measurement of this variability, as shown in Fig. 11. In order to assess whether our inferred star formation variability is enough to explain the abundance of UV-bright galaxies at $z > 10$, we perform a comparison with the model by A. Kravtsov & V. Belokurov (2024), where stochasticity of star formation is introduced in order to reproduce the observed UV luminosity functions at $z \approx 11 - 13$ and ≈ 16. They find that their model can successfully reproduce stellar masses and UV luminosities at those redshifts, after adopting only a modest lever of stochasticity of SFRs. Importantly, their models predict that the ratio between the SFRs averaged over 10 and 100 Myr ($R \equiv SFR_{10}/SFR_{100}$) should increase with redshift. This increase can be interpreted as galaxies becoming more bursty in the early Universe, and having on average rising SFHs. Fig. 13 shows the predictions from A. Kravtsov & V. Belokurov (2024), computed at $z = 5$ and 7, along with galaxies in redshift bins around these values, as indicated in the title of each panel. The grey circles show our PROSPECTOR-inferred measurements for all the galaxies in our original sample (i.e. without making a cut in stellar mass). The white points and error bars show the medians per UV magnitude bin (from $M_{UV} = -16$ to -24), plotted at the median M_{UV} of each bin. The errors reflect the number of galaxies contained in each bin. Finally, the blue curve and the shaded areas represent the extrapolated models with their corresponding 68 and 95 percentiles. As can be seen in the figure, our median PROSPECTOR-inferred measurements per M_{UV} bin are within the range of the model predictions. Moreover, the models predict an increase in R from $z = 5$ to 7 by a factor of $\approx 1.2 \pm 0.2$, while our measurements of R increase by a factor of $\approx 1.6 \pm 0.5$. Therefore, we find that the predictions from A. Kravtsov & V. Belokurov (2024) are consistent with this work at $z < 9$.
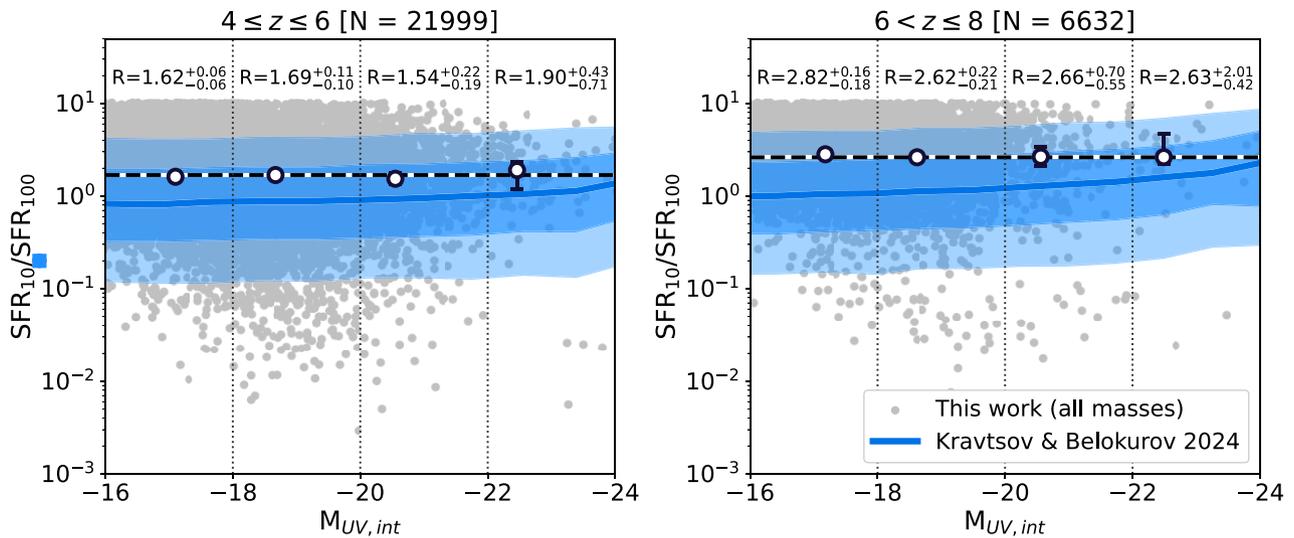
Figure 13. Ratio of SFRs averaged over 10 and 100 Myr, respectively ($R \equiv \mathrm{SFR_{10}/SFR_{100}}$), as a function of intrinsic UV magnitude. The scatter plots show the median measurements for galaxies in our sample, the upper limit of $R = 10$ is given by the maximum SFR per each time-scale ($\frac{1}{t_{\mathrm{average}}}$). The white circles with black edges show the median values for each UV magnitude bin (delimited by vertical dotted lines), the error bars reflect the number of galaxies in each bin and are obtained via bootstrapping. The median $\mathrm{SFR_{10}/SFR_{100}}$ values increase as a function of redshift, as highlighted by the horizontal dashed lines (and corresponding values of the ratio). The blue filled curves and shaded areas represent the models from A. Kravtsov & V. Belokurov (2024), with their 68 and 98 percentiles, computed at $z = 5$ and 7, respectively. We find that the models are able to reproduce our PROSPECTOR-inferred values.

We investigate the UV variability by measuring σ_{UV}, which describes the scatter in M_{UV} at fixed stellar mass. It should be emphasized that σ_{UV} can encapsulate information beyond burstiness of star formation. For example, it includes the scatter in the $M_\star$–M_{halo} conversion (since in some models σ_{UV} is defined at fixed halo mass), the long-time-scale diversity of SFHs at a fixed stellar mass, and the translation from SFHs to UV luminosities. The latter contains possible scatter from metallicity, nebular contribution, IMF variations, SFH assumptions, and, importantly, dust attenuation. Therefore, a large σ_{UV} does not necessarily mean burstier SFHs, since it can arise from several other factors.

Fig. 14 shows the dust-corrected σ_{UV} as a function of stellar mass for two redshift bins, $3 \leq z \leq 6$ and $6 < z \leq 9$. The grey shaded area represents the minimum σ_{UV} from X. Shen et al. (2023), needed to match observational constraints at $z \sim 9$, and the lower and upper boundaries show σ_{UV} with and without dust corrections, respectively. For comparison, and motivated by the agreement of the A. Kravtsov & V. Belokurov (2024) models with our galaxy properties, we include the σ_{UV} needed in their work in order to reproduce the observed UV luminosity functions at $5 < z < 10$ ($\sigma_{\mathrm{UV}} \approx 0.75$), and at $11 < z < 13$ ($\sigma_{\mathrm{UV}} \approx 1 - 1.3$), as blue dotted lines and shaded area. We find $\sigma_{\mathrm{UV}} \approx 0.75$ for our dust-corrected measurements in both redshift bins, with little-to-no dependence on stellar mass. This result agrees remarkably well with the minimum σ_{UV} from X. Shen et al. (2023) and the predictions including stochastic star formation from A. Kravtsov & V. Belokurov (2024), as well as the simulation-based studies from A. Pallottini & A. Ferrara (2023) and V. A. Semenov, C. Conroy & L. Hernquist (2025), in our redshift range (for a compilation of simulation results for high-redshift galaxies as a function of halo mass, see fig. 4 of X. Shen et al. 2024). Moreover, W. McClymont et al. (2025a) use THESAN-ZOOM simulated galaxies to measure the UV variability up to $z = 15$ (without accounting for dust attenuation), and find that at $z > 6$ their σ_{UV} converges to ≈ 0.75. Importantly, if we combine our estimations at $3 < z < 9$ with their measurements at $9 < z < 15$, we find a consistent picture

of $\sigma_{\mathrm{UV}} \approx 0.75$, with virtually no redshift evolution (a result that is also in agreement with other studies, e.g. L. Ciesla et al. 2024; M. Shuntov et al. 2025). W. McClymont et al. (2025a) explain this behaviour due to the UV tracing long-term scatter, which is only introduced as cosmic time increases.

To understand if the *JWST* observations at $z > 10$ can be explained by the UV variability, we show the analytic scatter estimated by V. Gelli, C. Mason & C. C. Hayward (2024, grey dot–dashed line), which is needed to reproduce UV luminosity functions up to $z = 14$ when adopting the THESAN-ZOOM star formation efficiency, as shown in X. Shen et al. (2025). A comparison between our estimated σ_{UV} and the measurements from W. McClymont et al. (2025a), with the X. Shen et al. (2025) limit, suggests that additional scatter is needed at lower stellar masses to explain the overabundance of observed UV-bright galaxies at $z > 10$. Thus, we find that the UV variability we measure at $z = 3 - 9$ is not enough to explain the UV luminosity functions at $z > 10$ (see also C. Carvajal-Bohorquez et al. 2025). Possible ways to address this issue include, for example, to invoke a top-heavy IMF (X. Shen et al. 2023; V. Mauerhofer et al. 2025), variable star formation efficiencies (A. Dekel et al. 2023; R. S. Somerville et al. 2025), or a UV variability that evolves strongly with redshift (A. Kravtsov & V. Belokurov 2024). Additionally, our measurements at the lowest stellar masses may underestimate the true effect due to sample incompleteness.

6.2 Implications on stellar mass completeness

In Section 3.2, we estimate the stellar mass completeness of our sample assuming constant mass-to-light ratios for a fixed *F444W* magnitude. We argue that this is a lower limit, and define partially complete and complete regions based on the shape of the sSFR as a function of stellar mass (see Fig. 4). By analysing the scatter of the SFMS, we find that SFHs are bursty on average, but more so at low stellar masses. Therefore, in this section, we explore the
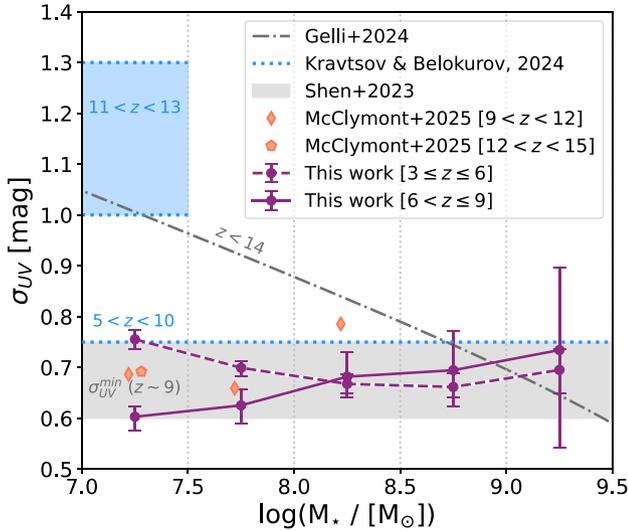
Figure 14. UV variability as a function of stellar mass for two redshift bins: $3 \leq z \leq 6$ (purple dashed) and $6 < z \leq 9$ (purple filled). Our measurements have been corrected for dust attenuation and the SED errors have been subtracted in quadrature. The UV traces longer time-scales, and as such, is less sensitive to the stellar mass limits used. The grey shaded area shows the minimum UV variability needed to reproduce observations at $z \approx 9$ from X. Shen et al. (2023), its lower (upper) bound represents dust corrected (uncorrected) values. The blue dotted horizontal lines and region show the σ_{UV} needed to reproduce UV luminosity functions at $5 < z < 10$ and $11 < z < 13$ from A. Kravtsov & V. Belokurov (2024), when a moderate amount of stochasticity in star formation is introduced. The diamonds and pentagon show the σ_{UV} values for $9 < z < 15$ from W. McClymont et al. (2025a). Finally, the dot–dashed grey line shows the analytic scatter estimated by V. Gelli et al. (2024), that was shown to reproduce the *JWST* observations up to $z = 14$, when THESAN-ZOOM star formation efficiencies are adopted (X. Shen et al. 2025). We find that our dust corrected UV variability converges at ≈ 0.75, in tight agreement with the σ_{UV}^{min} from X. Shen et al. (2023) and the models from A. Kravtsov & V. Belokurov (2024). However, more UV variability is required at lower stellar masses in order to explain the observed overabundance of UV-bright galaxies at $z > 10$.

implications that bursty star formation has on estimations of stellar mass completeness.

We have shown in Fig. 2 that PROSPECTOR can predict Hα and [O III]$_{\lambda 5007}$ emission line fluxes for a subsample of galaxies with *JWST* NIRSpec measurements from JADES, which means that recent SFRs can also be reliably estimated for these galaxies. Although promising, this result is based on a subsample composed of galaxies with detectable emission lines, and as such, is not representative of the entire galaxy population. Before making conclusions about stellar mass completeness methods, we first investigate if the partially complete region is due to PROSPECTOR limitations. Specifically, we consider if the code struggles with retrieving SFHs (and therefore, SFRs) when stellar masses and SFRs are low. In order to test this, we produce mock observations for two galaxies with $\log(M_\star/M_\odot) \approx 7.5$, with no recent star formation, and at the extremes of our redshift range. We decide to select a stellar mass below our derived stellar mass completeness limits to ensure the reliability of our method. The results are shown in Appendix C, and demonstrate that PROSPECTOR can indeed recover declining SFHs for low-mass galaxies even in the absence of medium-band photometry. Therefore, the partially complete region cannot be explained by limitations in our SED modelling routine.

After demonstrating that PROSPECTOR can retrieve galaxy properties remarkably well at the masses and redshifts used in this work, we now focus on the behaviour of the mass-to-light ratio of the galaxies in our sample, for a given stellar mass. Fig. 15 shows this ratio for galaxies with $\log(M_\star/M_\odot) = 8.0 - 8.5$, which is well represented at all redshifts studied here. For each redshift, we divide galaxies into three bins depending on their distance to the SFMS. In particular, we show galaxies above ($\Delta_{MS} \geq 0.5$), on ($-0.5 < \Delta_{MS} < 0.5$), and below ($\Delta_{MS} \leq -0.5$) this relation. We find that the mass-to-light ratio varies as a function of Δ_{MS} for a given stellar mass, and thus, that the assumption that the galaxies at the magnitude limit have the same mass-to-light ratio as the galaxies below it might be too simplistic (Section 3.2). As a consequence, the stellar mass completeness limits derived under this assumption are optimistic and should be used with caution, especially when star formation is bursty in nature (G. Sun et al. 2023a).

The process of fitting the SFMS is highly sensitive to the stellar mass completeness of the sample. If low-mass galaxies with low SFRs are missed, then the overall effect is that sSFRs depend negatively on stellar mass, since the relation becomes dominated by low-mass galaxies with recent star formation. This is illustrated by the piecewise fits in Fig. 5, which show that the slope of the relation between sSFR and stellar mass becomes negative when adopting the stellar mass limits derived following L. Pozzetti et al. (2010). W. McClymont et al. (2025a) study the implications that this observational bias has on the shape and evolution of the SFMS. Interestingly, they find that when the stellar mass completeness is not properly assessed, the SFMS evolution with redshift is less steep, mimicking the flattening seen in $z < 6$ observational studies such as J. S. Speagle et al. (2014) and P. Popesso et al. (2023).

In this work, we fit the SFMS in the stellar mass range where the sSFR for each time-scale is flat (see Fig. 4). Presenting an alternative mass completeness estimation method is outside of the scope of this study, however, we caution future observational studies to look carefully into this subject when fitting the SFMS. Thanks to facilities such as the *JWST*, and large surveys like JADES, having statistical samples of galaxies in the early Universe is now possible.

6.3 Implications for reionization

One of the major ongoing debates in cosmology is pinpointing which sources are mainly responsible for ionizing the Universe by $z \sim 5 - 6$: star-forming galaxies or AGN. Before the launch of the *JWST*, the community widely agreed on young stars in star-forming galaxies as being the dominant source of ionizing photons in the early Universe (e.g. S. Hassan et al. 2018; J. Rosdahl et al. 2018; M. Trebitsch et al. 2020; J. Chisholm et al. 2022). However, ever since the launch of this telescope, a population of low luminosity AGN has been unveiled (I. Juodžbalis et al. 2023; R. Maiolino et al. 2024; H. Übler et al. 2024), reigniting this debate. Although most works find that AGN are subdominant to the reionization process (P. Dayal et al. 2025; D. Jiang et al. 2025; S. Asthana et al. 2025), some find the opposite (see e.g. A. Grazian et al. 2024; P. Madau et al. 2024). In the context of star-forming galaxies as the main agents of reionisation, faint low-mass galaxies with bursty SFHs have been proposed to be key agents during the EoR (e.g. L. T. C. Seeyave et al. 2023; P. Rinaldi et al. 2024; C. Simmonds et al. 2024a, b; N. Choustikov et al. 2025), but see also R. P. Naidu et al. (2020). It is important to highlight that for galaxies to be able to ionise the Universe, the LyC radiation produced in their interiors must escape the ISM to reach the IGM. High LyC escape fractions (f_{esc}) have been directly observed (e.g. S. Borthakur et al. 2014; E. Vanzella et al. 2018; Y. I. Izotov et al. 2021; J. Kerutt
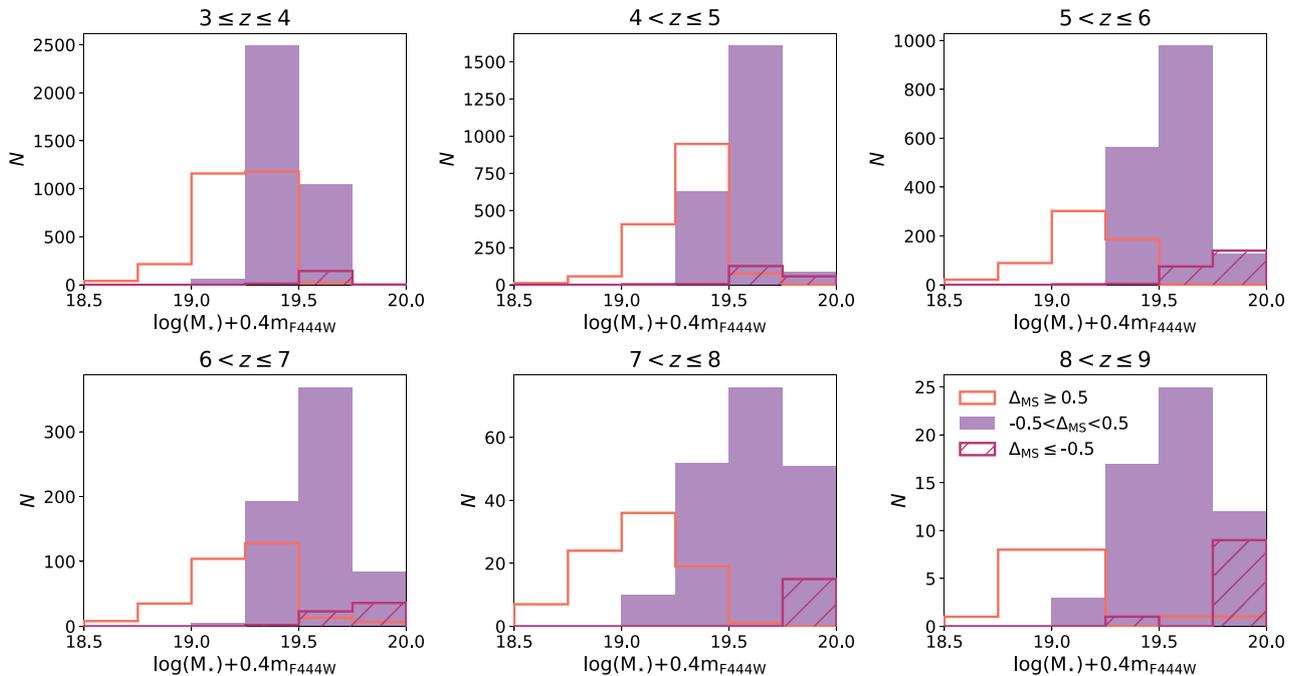
Figure 15. Mass-to-light ratio for galaxies with $\log(M_\star/M_\odot) = 8.0 - 8.5$, per redshift bin. In each panel we divide galaxies into three bins depending on their location respective to the SFMS: above ($\Delta_{\mathrm{MS}} \geq 0.5$, orange), on ($-0.5 < \Delta_{\mathrm{MS}} < 0.5$, purple filled), and below ($\Delta_{\mathrm{MS}} \leq -0.5$, red hatched) the relation, respectively. We find a clear dependence of the mass-to-light ratio on Δ_{MS}, where galaxies above the SFMS are brighter. Therefore, the assumption that the galaxies at the magnitude limit have the same mass-to-light ratio as the galaxies below it might be too simplistic, explaining why the region with $\log(M_\star/M_\odot) \approx 8.1 - 9.0$ is only partially complete.

et al. 2024), but usually not in large samples (E. Leitet et al. 2013; C. Leitherer et al. 2016; C. C. Steidel et al. 2018; S. R. Flury et al. 2022). Moreover, this radiation can only be measured up to $z \sim 5$ due to the increasingly neutral IGM (P. Madau 1995; A. K. Inoue et al. 2014), making f_{esc} the most elusive ingredient in studies regarding the sources responsible for the EoR.

A common way to investigate which galaxies are responsible for the reionization of the Universe is through the ionizing photon production efficiency, ξ_{ion}, given by the ratio between the ionizing photon flux and the non-ionizing UV continuum luminosity. Given the challenges in measuring ionizing photons in galaxies, ξ_{ion} is usually estimated by assuming Case-B recombination (i.e. no escape of ionizing radiation, $\xi_{\mathrm{ion},0}$). This property has been thoroughly investigated in the literature (e.g. R. J. Bouwens et al. 2016; A. L. Faisst et al. 2019; M. Stefanon et al. 2022; R. Endsley et al. 2023; G. Prieto-Lyon et al. 2023). Not surprisingly, $\xi_{\mathrm{ion},0}$ correlates with $\mathrm{SFR}_{10}/\mathrm{SFR}_{100}$ (C. Simmonds et al. 2023). In Fig. 5, we show the best fit to the SFMS using the SFR averaged over the past 10 Myr, and colour-coded by $\xi_{\mathrm{ion},0}$. The resulting colour gradient that can be seen indicates that this property also correlates with the distance to the SFMS, Δ_{MS}, where the galaxies that are more efficient producers of ionizing radiation are also the ones that lie above the SFMS, and are likely the type of galaxy dominating the ionization of the Universe.

Tying this work to the results from C. Simmonds et al. (2023, 2024b), through our study of the SFMS, we confirm that galaxies with stellar masses $\log(M_\star/M_\odot) = 8.0 - 10.0$ have bursty star formation. Moreover, we find that galaxies with $8.0 \leq \log(M_\star/M_\odot) \leq 8.5$ have a higher short-term scatter, indicating increased burstiness. Therefore, our work supports the scenario of low-mass galaxies with

bursty star formation being responsible for the bulk of the ionizing photon budget in the early Universe. We expect our results can be extrapolated to lower stellar masses, however, we caution that we are not complete below $\log(M_\star/M_\odot) \sim 8.0$. Finally, in light of our new insights into stellar mass completeness, we re-fit the ξ_{ion} relations from C. Simmonds et al. (2024b) using only galaxies with $\log(M_\star/M_\odot) \geq 9.0$ and find that the main conclusions of the work remain unchanged within errors, where ξ_{ion} depends on redshift and M_{UV} as:

$$\log(\xi_{\mathrm{ion}}(z, M_{\mathrm{UV}})) = (-0.003 \pm 0.015)z$$
$$+ (-0.019 \pm 0.015)M_{\mathrm{UV}} + (24.882 \pm 0.310).$$

This indicates that even though the SFMS is extremely sensitive to the stellar mass completeness of the sample, studies on the ionizsing properties of galaxies can be performed using less conservative stellar mass completeness estimates.

7 CAVEATS AND LIMITATIONS

The first and most important source of uncertainty in this work comes from the use of SED modelling, and the properties that are derived from this process. Importantly, it is challenging to measure individual SFHs, since to do so it is necessary to break degeneracies between indicators of burstiness (such as $\mathrm{SFR}_{10}/\mathrm{SFR}_{100}$) from parameters like dust attenuation, metallicity, and ionisation parameter (B. D. Johnson et al. 2013; A. Broussard et al. 2019). Although, we note that mid-infrared observations obtained with MIRI can aid in estimating physical properties of galaxies at high-redshift star-forming galaxies (J. M. Helton et al. 2025a). In a recent work, B. Wang et al. (2025) study the recovery of SFRs when adopting different SFH priors,

and find that although SFRs averaged over the past 30 Myr can be reasonable well recovered (with a median offset of ~ 0.1 dex), that fluctuations at shorter time-scales are not well captured, and that bursty star formation must be taken into account. Besides these complications, SED-fitting codes struggle to find reliable SFHs at $z > 7$ when older stellar populations are outshone by recent star formation (C. Papovich et al. 2023; S. Tacchella et al. 2023; R. Endsley et al. 2024; D. Narayanan et al. 2024; C. Witten et al. 2025).

In addition to these difficulties, a prior for the SFH must be assumed. We adopt a non-parametric continuity prior (J. Leja et al. 2019), consisting of eight bins of star formation, where the ratio between these bins is fit with a Student's *t*-distribution prior with a scale of 0.3. The latter means that some burstiness is allowed between adjacent bins, and that both star-forming and quenched galaxies can be reproduced (J. Leja et al. 2019; B. D. Johnson et al. 2021; P. Haskell et al. 2023), but that extreme solutions are not preferred. As a result, the burstiness found in this work might be underestimated, although the exact implications of using this SFH are not here explored. Promisingly, the continuity SFH used in this work has been shown to be less prone to outshining (B. Wang et al. 2025). Besides all the caveats introduced by the SED-fitting process itself, as in C. Simmonds et al. (2024b), we assume a Chabrier IMF, with a maximum stellar mass of 100 M$_\odot$. This choice of IMF was motivated by the size of the sample, in the hope of selecting a prescription that represents the whole data set. However, this IMF might not be the best option if more extreme stellar populations are required (e.g. a top-heavy IMF, as in A. J. Cameron et al. 2024), if the IMF depends on the physical properties of the gas in each individual galaxy (M. Haslbauer et al. 2024; P. Kroupa et al. 2026; A. H. Zonoozi, H. Haghi & P. Kroupa 2025), or if the IMF evolves as a function of cosmic time.

Secondly, as mentioned in the previous section, ever since the launch of the *JWST*, a significant population of low-luminosity AGN at high redshifts has been discovered (I. Juodžbalis et al. 2023; P. Madau et al. 2024; R. Maiolino et al. 2024; H. Übler et al. 2024; J. Scholtz et al. 2025). We removed the *JWST* MIRI selected AGN from J. Lyu et al. (2024) and the broad-line AGN from I. Juodžbalis et al. (2025) to avoid contamination from these sources, however, it is possible that our sample contains other AGN, which would lead to our stellar masses being overestimated in these cases (J. Buchner et al. 2024). Unfortunately, it is virtually impossible to reliably identify AGN with photometry alone (E. J. Wasleske & V. F. Baldassare 2024). As such, we caution the reader that our sample might contain AGN when their emission can be mimicked by stellar emission.

Finally, our work relies on photometric redshifts. In particular, we use EAZY redshifts as priors for our PROSPECTOR fitting routine. The former has been proven to yield accurate results for large JADES samples using photometry as input (M. J. Rieke et al. 2023). In addition, the PROSPECTOR-inferred redshifts are in good (but not perfect) agreement with spectroscopic redshifts from literature (C. Simmonds et al. 2024b). This indicates that overall our photometric redshifts are reliable, but that some outliers are inevitably part of this work. We stress that this outlier fraction is small (of the order of at most a few percent). Moreover, our imposed χ^2 cut should ensure that the data are well reproduced by our best-fitting models.

As a summary, although there are limitations to our methods since they rely on photometry, photometric redshifts, and SED modelling, they are – as much as possible – accurate and representative of the galaxy population at $3 \le z \le 9$.

8 SUMMARY AND CONCLUSIONS

In this work, we have utilized NIRCam photometry of galaxies in the GOODS-N and GOODS-S fields at redshifts $3 < z < 9$, combined with galaxy properties inferred using the SED-fitting code PROSPECTOR, to study the SFMS and its scatter. We define two regions based on stellar mass: a partially complete region ($\log(M_\star/M_\odot) \approx 8.1 - 10.3$, with 18 344 galaxies) and a more conservative complete region ($\log(M_\star/M_\odot) = 9.0 - 10.3$, with 2989 galaxies). Given the sensitivity of the SFMS shape to the stellar mass completeness limit, we focus on fitting the SFMS in the complete region, extrapolating to lower masses when considering scatter.

Our main findings can be summarized briefly as:

(i) The SED modelling code PROSPECTOR is able to retrieve emission-line fluxes and SFHs reliably when adopting the continuity SFH prior, even in the absence of medium-band photometry.

(ii) The redshift dependence of the SFMS at an averaging time-scale of 10 Myr (sSFR$_{10}$) is $(1 + z)^\mu$ with $\mu = 2.30^{+0.03}_{-0.01}$, which is close to the sMAR onto dark matter for a ΛCDM cosmology in the Einstein–deSitter regime (A. Dekel et al. 2013) and overall consistent with predictions from numerical simulations (e.g. S. Tacchella et al. 2016a; W. McClymont et al. 2025a).

(iii) The SFMS normalization varies in a complex way with the SFR averaging time-scale, reflecting the combined effects of bursty star formation and increased prevalence of rising SFHs toward higher redshifts.

(iv) We find that the sSFR is nearly independent of stellar mass (e.g. SFR $\propto M_\star^\alpha$ with $\alpha \approx 1$) when completeness of the sample is taken into account, suggesting that galaxies with a variety of stellar masses double their mass on a similar time-scale. Our SFMS agrees in shape and behaviour with the one inferred using the THESAN-ZOOM simulation (W. McClymont et al. 2025a), suggesting that the flattening of the SFMS (e.g. $\alpha < 1$) found in previous studies up to $z \approx 6$ is likely due to incompleteness in stellar mass.

(v) Our analysis of the SFMS scatter indicates that galaxies in the mass range $\log(M_\star/M_\odot) = 8.0 - 10.0$ have bursty SFHs. Importantly, the short-term variability indicates that the burstiness is higher at lower stellar masses.

(vi) We observe no significant trend of stellar age and stellar mass with distance to the SFMS. On average, we find that massive (low-mass) galaxies are slightly older (younger), and that older (younger) galaxies tend to lie below (above) the SFMS, consistent with short-term fluctuations in star formation dominating the scatter of the SFMS.

(vii) We estimate the UV variability (σ_{UV}) to analyse the impact of bursty SFHs on the observed over-abundance of UV-bright galaxies at $z > 10$. We conclude that additional scatter must be introduced in order to explain these observations. This could be achieved by, for example, invoking a top-heavy IMF, variable star formation efficiencies, or significantly increasing the burstiness of star formation at $z > 9$.

(viii) We caution future studies about estimating stellar mass completeness limits that assume a constant mass-to-light ratio for a given stellar mass. We show that this ratio depends on the distance to the SFMS. Therefore, a conservative approach, such as the one adopted in this work, is suggested when studying the SFMS.

Overall, we confirm in this work that SFHs are bursty across cosmic time, with lower mass galaxies showing increased burstiness. In this work we aimed to answer two overarching questions: (1) how universal is the SFMS at early times? and, (2) what processes govern its emergence and evolution? We find that the SFMS is well in place

up to $z = 9$. Therefore, the emergence of the SFMS probably takes place at $z > 9$. In order to push into this redshift regime, we would need a stellar-mass complete sample of galaxies at $z \approx 9 - 14$. It is unclear if this will feasible in the near future, however, deeper imaging – especially including MIRI coverage – is needed (J. M. Helton et al. 2025b).

DATA AVAILABILITY

The data underlying this article will be shared on reasonable request to the corresponding author. Fully reduced NIRCam images and NIRSpec spectra are publicly available on MAST (https://archive.stsci.edu/hlsp/jades), with doi:10.17909/8tdj-8n28, doi:10.17909/z2gw-mk31, and doi:10.17909/fsc4-dt61 (M. J. Rieke et al. 2023; D. J. Eisenstein et al. 2023a; A. J. Bunker et al. 2024; F. D'Eugenio et al. 2025).

REFERENCES

Abramson L. E., Gladders M. D., Dressler A., Oemler A., Jr, Poggianti B., Vulcani B., 2016, ApJ, 832, 7

Abramson L. E., Kelson D. D., Dressler A., Poggianti B., Gladders M. D., Oemler A., Jr, Vulcani B., 2014, ApJ, 785, L36

Adams N. J. et al., 2024, ApJ, 965, 169

Anglés-Alcázar D., Faucher-Giguère C.-A., Kereš D., Hopkins P. F., Quataert E., Murray N., 2017, MNRAS, 470, 4698

Appleby S., Davé R., Kraljic K., Anglés-Alcázar D., Narayanan D., 2020, MNRAS, 494, 6053

Asada Y. et al., 2024, MNRAS, 527, 11372

Asthana S., Haehnelt M. G., Kulkarni G., Bolton J. S., Gaikwad P., Keating L. C., Puchwein E., 2025, MNRAS, 542, 2968

Atek H., Furtak L. J., Oesch P., van Dokkum P., Reddy N., Contini T., Illingworth G., Wilkins S., 2022, MNRAS, 511, 4464

Baker W. M. et al., 2023, MNRAS, 518, 4767

Baker W. M. et al., 2025a, A&A, 697, A90

Baker W. M. et al., 2025b, A&A, 702, A270

Bauer A. E., Conselice C. J., Pérez-González P. G., Grützbauch R., Bluck A. F. L., Buitrago F., Mortlock A., 2011, MNRAS, 417, 289

Behroozi P. S., Wechsler R. H., Conroy C., 2013, ApJ, 770, 57

Belfiore F. et al., 2018, MNRAS, 477, 3014

Benincasa S. M. et al., 2020, MNRAS, 497, 3993

Boogaard L. A. et al., 2018, A&A, 619, A27

Borthakur S., Heckman T. M., Leitherer C., Overzier R. A., 2014, Science, 346, 216

Bosman S. E. I. et al., 2022, MNRAS, 514, 55

Bouché N. et al., 2010, ApJ, 718, 1001

Bouwens R. J., Smit R., Labbé I., Franx M., Caruana J., Oesch P., Stefanon M., Rasappu N., 2016, ApJ, 831, 176

Boyett K. et al., 2024, MNRAS, 535, 1796

Bradley L. et al., 2022, astropy/photutils: 1.5.0, Zenodo. Available at: https://doi.org/10.5281/zenodo.6825092

Brammer G. B., van Dokkum P. G., Coppi P., 2008, ApJ, 686, 1503

Brinchmann J., Charlot S., White S. D. M., Tremonti C., Kauffmann G., Heckman T., Brinkmann J., 2004, MNRAS, 351, 1151

Broussard A. et al., 2019, ApJ, 873, 74

Buchner J. et al., 2024, A&A, 692, A161

Bunker A. J. et al., 2024, A&A, 690, A288

Calzetti D., Kinney A. L., Storchi-Bergmann T., 1994, ApJ, 429, 582

Cameron A. J. et al., 2023, A&A, 677, A115

Cameron A. J., Katz H., Witten C., Saxena A., Laporte N., Bunker A. J., 2024, MNRAS, 534, 523

Caplar N., Tacchella S., 2019, MNRAS, 487, 3845

Carniani S. et al., 2024, Nature, 633, 318

Carvajal-Bohorquez C. et al., 2025, preprint (arXiv:2507.13160)

Casey C. M. et al., 2024, ApJ, 965, 98

Castellano M. et al., 2022, ApJ, 938, L15

Cenci E., Feldmann R., Gensior J., Moreno J., Bassini L., Bernardini M., 2024, MNRAS, 527, 7871

Chabrier G., 2003, PASP, 115, 763

Charlot S., Fall S. M., 2000, ApJ, 539, 718

Chen Y.-M., Wild V., Kauffmann G., Blaizot J., Davis M., Noeske K., Wang J.-M., Willmer C., 2009, MNRAS, 393, 406

Chevallard J., Charlot S., 2016, MNRAS, 462, 1415

Chisholm J. et al., 2022, MNRAS, 517, 5104

Choi J., Dotter A., Conroy C., Cantiello M., Paxton B., Johnson B. D., 2016, ApJ, 823, 102

Choustikov N., Stiskalek R., Saxena A., Katz H., Devriendt J., Slyz A., Subdepartment of Astrophysics U. o. O., 2025, MNRAS, 537, 2273

Ciesla L. et al., 2024, A&A, 686, A128

Clarke L., Shapley A. E., Sanders R. L., Topping M. W., Brammer G. B., Bento T., Reddy N. A., Kehoe E., 2024, ApJ, 977, 133

Cole J. W. et al., 2025, ApJ, 979, 193

Conroy C., 2013, ARA&A, 51, 393

Conroy C., Gunn J. E., 2010, Astrophysics Source Code Library, record ascl:1010.043

Conroy C., Gunn J. E., White M., 2009, ApJ, 699, 486

Curtis-Lake E. et al., 2023, Nat. Astron., 7, 622

Curtis-Lake E., Chevallard J., Charlot S., Sandles L., 2021, MNRAS, 503, 4855

D'Eugenio F. et al., 2024, A&A, 689, A152

D'Eugenio F. et al., 2025, ApJS, 277, 4

D'Silva J. C. J., Lagos C. D. P., Davies L. J. M., Lovell C. C., Vijayan A. P., 2023, MNRAS, 518, 456

Daddi E. et al., 2007, ApJ, 670, 156

Daddi E. et al., 2010, ApJ, 713, 686

Daddi E. et al., 2022, A&A, 661, L7

Davies L. J. M. et al., 2019, MNRAS, 483, 1881

Davies L. J. M. et al., 2025a, MNRAS, 540, 1870

Davies L. J. M. et al., 2025b, MNRAS, 541, 573

Dayal P. et al., 2025, A&A, 697, A211

Dekel A., Sarkar K. C., Birnboim Y., Mandelker N., Li Z., 2023, MNRAS, 523, 3201

Dekel A., Zolotov A., Tweed D., Cacciato M., Ceverino D., Primack J. R., 2013, MNRAS, 435, 999

Di Matteo P., Combes F., Melchior A. L., Semelin B., 2007, A&A, 468, 61

Dome T., Tacchella S., Fialkov A., Ceverino D., Dekel A., Ginzburg O., Lapiner S., Looser T. J., 2024, MNRAS, 527, 2139

Domínguez A., Siana B., Brooks A. M., Christensen C. R., Bruzual G., Stark D. P., Alavi A., 2015, MNRAS, 451, 839

Donnan C. T. et al., 2024, MNRAS, 533, 3222

Donnan C. T., McLeod D. J., McLure R. J., Dunlop J. S., Carnall A. C., Cullen F., Magee D., 2023, MNRAS, 520, 4554

Donnari M. et al., 2019a, MNRAS, 485, 4817

Donnari M. et al., 2019b, MNRAS, 489, 3036

Dotter A., 2016, ApJS, 222, 8

Duan Q. et al., 2024, preprint (arXiv:2411.04944)

Eisenstein D. J. et al., 2023a, preprint (arXiv:2306.02465)

Eisenstein D. J. et al., 2023b, preprint (arXiv:2310.12340)

Elbaz D. et al., 2007, A&A, 468, 33

Elbaz D. et al., 2011, A&A, 533, A119

Emami N. et al., 2021, ApJ, 922, 217

Emami N., Siana B., Weisz D. R., Johnson B. D., Ma X., El-Badry K., 2019, ApJ, 881, 71

Endsley R. et al., 2024, MNRAS, 533, 1111

Endsley R., Stark D. P., Whitler L., Topping M. W., Chen Z., Plat A., Chisholm J., Charlot S., 2023, MNRAS, 524, 2312

Erfanianfar G. et al., 2016, MNRAS, 455, 2839

Faisst A. L., Capak P. L., Emami N., Tacchella S., Larson K. L., 2019, ApJ, 884, 133

Faucher-Giguère C.-A., 2018, MNRAS, 473, 3717

Feldmann R., 2017, MNRAS, 470, L59

Ferland G. J. et al., 2013, Rev. Mex. Astron. Astrofis., 49, 137

Ferrara A., Pallottini A., Dayal P., 2023, MNRAS, 522, 3986

Ferruit P. et al., 2022, A&A, 661, A81

Finkelstein S. L. et al., 2023, ApJ, 946, L13

Flury S. R. et al., 2022, ApJS, 260, 1

Gardner J. P. et al., 2023, PASP, 135, 068001

Gelli V., Mason C., Hayward C. C., 2024, ApJ, 975, 192

Giavalisco M. et al., 2004, ApJ, 600, L93

Gladders M. D., Oemler A., Dressler A., Poggianti B., Vulcani B., Abramson L., 2013, ApJ, 770, 64

Grazian A. et al., 2024, ApJ, 974, 84

Grogin N. A. et al., 2011, ApJS, 197, 35

Guo K., Zheng X. Z., Fu H., 2013, ApJ, 778, 23

Guo K., Zheng X. Z., Wang T., Fu H., 2015, ApJ, 808, L49

Guo Y. et al., 2016, ApJ, 833, 37

Hainline K. N. et al., 2024, ApJ, 964, 71

Harikane Y. et al., 2023, ApJS, 265, 5

Harikane Y., Nakajima K., Ouchi M., Umeda H., Isobe Y., Ono Y., Xu Y., Zhang Y., 2024, ApJ, 960, 56

Haskell P., Smith D. J. B., Cochrane R. K., Hayward C. C., Anglés-Alcázar D., 2023, MNRAS, 525, 1535

Haslbauer M., Yan Z., Jerabkova T., Gjergo E., Kroupa P., Zonoozi A. H., 2024, A&A, 689, A221

Hassan S., Davé R., Mitra S., Finlator K., Ciardi B., Santos M. G., 2018, MNRAS, 473, 227

Hayward C. C. et al., 2014, MNRAS, 445, 1598

Hayward C. C., Hopkins P. F., 2017, MNRAS, 465, 1682

Helton J. M. et al., 2025a, preprint (arXiv:2506.02099)

Helton J. M. et al., 2025b, Nat. Astron., 9, 729

Herard-Demanche T. et al., 2025, MNRAS, 537, 788

Hopkins P. F. et al., 2023, MNRAS, 525, 2241

Hopkins P. F., Kereš D., Oñorbe J., Faucher-Giguère C.-A., Quataert E., Murray N., Bullock J. S., 2014, MNRAS, 445, 581

Illingworth G. et al., 2016, preprint (arXiv:1606.00841)

Inoue A. K., Shimizu I., Iwata I., Tanaka M., 2014, MNRAS, 442, 1805

Iyer K. G. et al., 2020, MNRAS, 498, 430

Izotov Y. I., Worseck G., Schaerer D., Guseva N. G., Chisholm J., Thuan T. X., Fricke K. J., Verhamme A., 2021, MNRAS, 503, 1734

Jakobsen P. et al., 2022, A&A, 661, A80

Ji Z. et al., 2024, ApJ, 974, 135

Jiang D., Jiang L., Sun S., Liu W., Fu S., 2025, Nat. Astron., Advanced Online Publication. Available at: https://doi.org/10.1038/s41550-025-02676-7

Johnson B. D. et al., 2013, ApJ, 772, 8

Johnson B. D., Leja J. L., Conroy C., Speagle J. S., 2019, Astrophysics Source Code Library, record ascl:1905.025

Johnson B. D., Leja J., Conroy C., Speagle J. S., 2021, ApJS, 254, 22

Juodžbalis I. et al., 2024, MNRAS, 525, 1353

Juodžbalis I. et al., 2025, preprint (arXiv:2504.03551)

Karim A. et al., 2011, ApJ, 730, 61

Kashino D. et al., 2013, ApJ, 777, L8

Katsianis A., Tescari E., Wyithe J. S. B., 2016, Publ. Astron. Soc. Aust., 33, e029

Kauffmann G., 2014, MNRAS, 441, 2717

Keating L. C., Weinberger L. H., Kulkarni G., Haehnelt M. G., Chardin J., Aubert D., 2020, MNRAS, 491, 1736

Kelson D. D., 2014, preprint (arXiv:1406.5191)

Kennicutt R. C., Jr, 1998, ARA&A, 36, 189

Kennicutt R. C., Evans N. J., 2012, ARA&A, 50, 531

Kerutt J. et al., 2024, A&A, 684, A42

Koekemoer A. M. et al., 2011, ApJS, 197, 36

Kokorev V. et al., 2025, ApJ, 988, L10

Kravtsov A., Belokurov V., 2024, preprint (arXiv:2405.04578)

Kriek M., Conroy C., 2013, ApJ, 775, L16

Kroupa P., Gjergo E., Jerabkova T., Yan Z., 2026, Encyclopedia of Astrophysics, Vol. 2, The Initial Mass Function of Stars. Elsevier, Amsterdam, Netherlands, p. 173

Kurczynski P. et al., 2016, ApJ, 820, L1

Langeroodi D., Hjorth J., 2024, preprint (arXiv:2404.13045)

Lapiner S. et al., 2023, MNRAS, 522, 4515

Lastennet E., Lejeune T., Oblak E., Westera P., Buser R., 2002, Ap&SS, 280, 83

Lee K.-S. et al., 2012, ApJ, 752, 66

Lee N. et al., 2015, ApJ, 801, 80

Leitet E., Bergvall N., Hayes M., Linné S., Zackrisson E., 2013, A&A, 553, A106

Leitherer C. et al., 1999, ApJS, 123, 3

Leitherer C., Hernandez S., Lee J. C., Oey M. S., 2016, ApJ, 823, 64

Leja J. et al., 2022, ApJ, 936, 165

Leja J., Carnall A. C., Johnson B. D., Conroy C., Speagle J. S., 2019, ApJ, 876, 3

Leslie S. K. et al., 2020, ApJ, 899, 58

Li Z., Dekel A., Sarkar K. C., Aung H., Giavalisco M., Mandelker N., Tacchella S., 2024, A&A, 690, A108

Lilly S. J., Carollo C. M., Pipino A., Renzini A., Peng Y., 2013, ApJ, 772, 119

Looser T. J. et al., 2025, A&A, 697, A88

Lyu J. et al., 2024, ApJ, 966, 229

Madau P., 1995, ApJ, 441, 18

Madau P., Dickinson M., 2014, ARA&A, 52, 415

Madau P., Giallongo E., Grazian A., Haardt F., 2024, ApJ, 971, 75

Magdis G. E., Elbaz D., Daddi E., Morrison G. E., Dickinson M., Rigopoulou D., Gobat R., Hwang H. S., 2010, ApJ, 714, 1740

Maiolino R. et al., 2024, A&A, 691, A145

Mason C. A., Trenti M., Treu T., 2023, MNRAS, 521, 497

Matthee J., Schaye J., 2019, MNRAS, 484, 915

Mauerhofer V., Dayal P., Haehnelt M. G., Kimm T., Rosdahl J., Teyssier R., 2025, A&A, 696, A157

McClymont W. et al., 2025a, MNRAS, 544, 513

McClymont W. et al., 2025b, MNRAS, 544, 1732

McLeod D. J. et al., 2024, MNRAS, 527, 5004

Mirocha J., Furlanetto S. R., 2023, MNRAS, 519, 843

Moustakas J. et al., 2013, ApJ, 767, 50

Muñoz J. B., Mirocha J., Furlanetto S., Sabti N., 2023, MNRAS, 526, L47

Naidu R. P. et al., 2022, ApJ, 940, L14

Naidu R. P. et al., 2025, preprint (arXiv:2505.11263)

Naidu R. P., Tacchella S., Mason C. A., Bose S., Oesch P. A., Conroy C., 2020, ApJ, 892, 109

Narayanan D. et al., 2024, ApJ, 961, 73

Neistein E., Dekel A., 2008, MNRAS, 383, 615

Noeske K. G. et al., 2007, ApJ, 660, L43

Oesch P. A. et al., 2023, MNRAS, 525, 2864

Oliver S. et al., 2010, MNRAS, 405, 2279

Pallottini A., Ferrara A., 2023, A&A, 677, L4

Pannella M. et al., 2009, ApJ, 698, L116

Papovich C. et al., 2023, ApJ, 949, L18

Papovich C., Dickinson M., Ferguson H. C., 2001, ApJ, 559, 620

Patel S. G., Holden B. P., Kelson D. D., Illingworth G. D., Franx M., 2009, ApJ, 705, L67

Paulino-Afonso A., Sobral D., Darvish B., Ribeiro B., Smail I., Best P., Stroe A., Cairns J., 2020, A&A, 633, A70

Pearson W. J. et al., 2018, A&A, 615, A146

Pflamm-Altenburg J., Weidner C., Kroupa P., 2009, MNRAS, 395, 394

Planck Collaboration VI, 2020, A&A, 641, A6

Popesso P. et al., 2019a, MNRAS, 483, 3213

Popesso P. et al., 2019b, MNRAS, 490, 5285

Popesso P. et al., 2023, MNRAS, 519, 1526

Pozzetti L. et al., 2010, A&A, 523, A13

Prieto-Lyon G. et al., 2023, A&A, 672, A186

Puskás D. et al., 2025, MNRAS, 540, 2146

Reddy N. A. et al., 2025, preprint (arXiv:2506.17396)

Reddy N. A., Steidel C. C., Fadda D., Yan L., Pettini M., Shapley A. E., Erb D. K., Adelberger K. L., 2006, ApJ, 644, 792

Reddy N. et al., 2012, ApJ, 744, 154

Ren K., Trenti M., Mason C. A., 2019, ApJ, 878, 114

Renzini A., Peng Y.-j., 2015, ApJ, 801, L29

Rieke M. J. et al., 2023, ApJS, 269, 16

Rinaldi P. et al., 2024, ApJ, 969, 12

Rinaldi P. et al., 2025, ApJ, 981, 161

Rinaldi P., Caputi K. I., van Mierlo S. E., Ashby M. L. N., Caminha G. B., Iani E., 2022, ApJ, 930, 128

Robertson B. E. et al., 2023, Nat. Astron., 7, 611

Robertson B. et al., 2024, ApJ, 970, 31

Robertson B., Bullock J. S., Cox T. J., Di Matteo T., Hernquist L., Springel V., Yoshida N., 2006, ApJ, 645, 986

Rodighiero G. et al., 2011, ApJ, 739, L40

Rodríguez-Puebla A., Primack J. R., Behroozi P., Faber S. M., 2016, MNRAS, 455, 2592

Rosa-González D., Terlevich E., Terlevich R., 2002, MNRAS, 332, 283

Rosdahl J. et al., 2018, MNRAS, 479, 994

Salim S. et al., 2007, ApJS, 173, 267

Salmi F., Daddi E., Elbaz D., Sargent M. T., Dickinson M., Renzini A., Bethermin M., Le Borgne D., 2012, ApJ, 754, L14

Salmon B. et al., 2015, ApJ, 799, 183

Salpeter E. E., 1955, ApJ, 121, 161

Sandles L., Curtis-Lake E., Charlot S., Chevallard J., Maiolino R., 2022, MNRAS, 515, 2951

Santini P. et al., 2009, A&A, 504, 751

Santini P. et al., 2017, ApJ, 847, 76

Scholtz J. et al., 2024, A&A, 687, A283

Scholtz J. et al., 2025, A&A, 697, A175

Schreiber C. et al., 2015, A&A, 575, A74

Seeyave L. T. C. et al., 2023, MNRAS, 525, 2422

Semenov V. A., Conroy C., Hernquist L., 2025, ApJ, 989, 219

Semenov V. A., Kravtsov A. V., Gnedin N. Y., 2017, ApJ, 845, 133

Shapley A. E., Sanders R. L., Reddy N. A., Topping M. W., Brammer G. B., 2023, ApJ, 954, 157

Shen S., Madau P., Conroy C., Governato F., Mayer L., 2014, ApJ, 792, 99

Shen X. et al., 2025, preprint (arXiv:2503.01949)

Shen X., Vogelsberger M., Boylan-Kolchin M., Tacchella S., Kannan R., 2023, MNRAS, 525, 3254

Shen X., Vogelsberger M., Boylan-Kolchin M., Tacchella S., Naidu R. P., 2024, MNRAS, 533, 3923

Sherman S. et al., 2021, MNRAS, 505, 947

Shim H., Chary R.-R., Dickinson M., Lin L., Spinrad H., Stern D., Yan C.-H., 2011, ApJ, 738, 69

Shin E.-j., Tacchella S., Kim J.-h., Iyer K. G., Semenov V. A., 2023, ApJ, 947, 61

Shivaei I. et al., 2015b, ApJ, 815, 98

Shivaei I., Reddy N. A., Steidel C. C., Shapley A. E., 2015a, ApJ, 804, 149

Shuntov M. et al., 2025, A&A, 699, A231

Simmonds C. et al., 2023, MNRAS, 523, 5468

Simmonds C. et al., 2024a, MNRAS, 527, 6139

Simmonds C. et al., 2024b, MNRAS, 535, 2998

Smit R., Bouwens R. J., Labbé I., Franx M., Wilkins S. M., Oesch P. A., 2016, ApJ, 833, 254

Sobral D., Best P. N., Smail I., Mobasher B., Stott J., Nisbet D., 2014, MNRAS, 437, 3516

Somerville R. S., Yung L. Y. A., Lancaster L., Menon S., Sommovigo L., Finkelstein S. L., 2025, MNRAS, preprint (arXiv:2505.05442)

Speagle J. S., Steinhardt C. L., Capak P. L., Silverman J. D., 2014, ApJS, 214, 15

Stefanon M., Bouwens R. J., Illingworth G. D., Labbé I., Oesch P. A., Gonzalez V., 2022, ApJ, 935, 94

Steidel C. C., Bogosavljević M., Shapley A. E., Reddy N. A., Rudie G. C., Pettini M., Trainor R. F., Strom A. L., 2018, ApJ, 869, 123

Steinhardt C. L. et al., 2014, ApJ, 791, L25

Stinson G. S., Dalcanton J. J., Quinn T., Kaufmann T., Wadsley J., 2007, ApJ, 667, 170

Sun F. et al., 2024, ApJ, 961, 69

Sun G., Faucher-Giguère C.-A., Hayward C. C., Shen X., 2023a, MNRAS, 526, 2665

Sun G., Faucher-Giguère C.-A., Hayward C. C., Shen X., Wetzel A., Cochrane R. K., 2023b, ApJ, 955, L35

Tacchella S. et al., 2022a, MNRAS, 513, 2904

Tacchella S. et al., 2022b, ApJ, 927, 170

Tacchella S. et al., 2023, MNRAS, 522, 6236

Tacchella S., Bose S., Conroy C., Eisenstein D. J., Johnson B. D., 2018, ApJ, 868, 92

Tacchella S., Dekel A., Carollo C. M., Ceverino D., DeGraf C., Lapiner S., Mandelker N., Primack J. R., 2016b, MNRAS, 458, 242

Tacchella S., Dekel A., Carollo C. M., Ceverino D., DeGraf C., Lapiner S., Mandelker N., Primack Joel R., 2016a, MNRAS, 457, 2790

Tacchella S., Forbes J. C., Caplar N., 2020, MNRAS, 497, 698

Tacchella S., Trenti M., Carollo C. M., 2013, ApJ, 768, L37

Tacconi L. J. et al., 2013, ApJ, 768, 74

Tacconi L. J., Genzel R., Sternberg A., 2020, ARA&A, 58, 157

Tan J. C., 2000, ApJ, 536, 173

Tasca L. A. M. et al., 2015, A&A, 581, A54

Tasker E. J., 2011, ApJ, 730, 11

Teyssier R., Chapon D., Bournaud F., 2010, ApJ, 720, L149

Thorne J. E. et al., 2021, MNRAS, 505, 540

Tomczak A. R. et al., 2016, ApJ, 817, 118

Trebitsch M., Volonteri M., Dubois Y., 2020, MNRAS, 494, 3453

Trinca A., Schneider R., Valiante R., Graziani L., Ferrotti A., Omukai K., Chon S., 2024, MNRAS, 529, 3563

Übler H. et al., 2024, MNRAS, 531, 355

Utomo D., Kriek M., Labbé I., Conroy C., Fumagalli M., 2014, ApJ, 783, L30

Vanzella E. et al., 2018, MNRAS, 476, L15

Vazdekis A. et al., 2015, MNRAS, 449, 1177

Wan J. T., Tacchella S., D'Eugenio F., Johnson B. D., van der Wel A., 2025, MNRAS, 539, 2891

Wan J. T., Tacchella S., Johnson B. D., Iyer K. G., Speagle J. S., Maiolino R., 2024, MNRAS, 532, 4002

Wang B. et al., 2024, ApJ, 963, 74

Wang B. et al., 2025, ApJ, 987, 184

Wang E., Lilly S. J., 2020, ApJ, 895, 25

Wasleske E. J., Baldassare V. F., 2024, ApJ, 971, 68

Weibel A. et al., 2025, preprint (arXiv:2507.06292)

Weisz D. R. et al., 2012, ApJ, 744, 44

Weisz D. R., Dolphin A. E., Skillman E. D., Holtzman J., Gilbert K. M., Dalcanton J. J., Williams B. F., 2014, ApJ, 789, 147

Whitaker K. E. et al., 2014, ApJ, 795, 104

Whitaker K. E. et al., 2019, ApJS, 244, 16

Whitaker K. E., Pope A., Cybulski R., Casey C. M., Popping G., Yun M. S., 2017, ApJ, 850, 208

Whitaker K. E., van Dokkum P. G., Brammer G., Franx M., 2012, ApJ, 754, L29

Whitler L. et al., 2025, ApJ, 992, 63

Williams C. C. et al., 2023, ApJS, 268, 64

Williams C. C. et al., 2024, ApJ, 968, 34

Witten C. et al., 2025, MNRAS, 537, 112

Yeh J. Y. C. et al., 2023, MNRAS, 520, 2757

Zahid H. J., Bresolin F., Kewley L. J., Coil A. L., Davé R., 2012, ApJ, 750, 120

Zhu Y. et al., 2024, MNRAS, 533, L49

Zolotov A. et al., 2015, MNRAS, 450, 2327

Zonoozi A. H., Haghi H., Kroupa P., 2025, MNRAS, 537, 2782

SUPPORTING INFORMATION

Supplementary data are available at *MNRAS* online.

author_list_SFMS.pdf

Please note: Oxford University Press is not responsible for the content or functionality of any supporting materials supplied by the authors. Any queries (other than missing material) should be directed to the corresponding author for the article.

APPENDIX A: COMPARING STAR FORMATION RATES

Comparison of the SFRs averaged over the past 10 Myr (SFR_{10}) with those derived from the Hα dust-corrected luminosities using
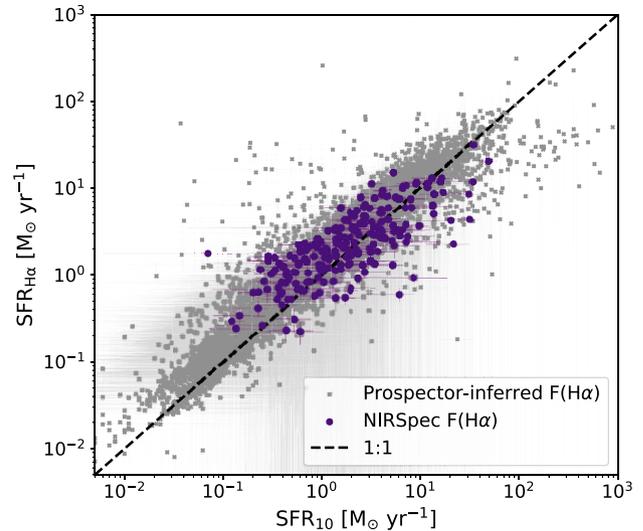

Figure A1. $SFR_{H\alpha}$ versus SFR_{10} for all galaxies in our sample with $8.0 \leq \log(M_\star/M_\odot) \leq 10.3$ (grey crosses, using PROSPECTOR-inferred Hα fluxes), and for the subsample with NIRSpec measurements (purple circles). The dashed black line shows the 1:1 relation, and confirms that SFR_{10} traces recent star formation, as seen by Hα emission.

the dust-corrected Hα luminosity conversion from I. Shivaei et al. (2015a). This SFR conversion was estimated based on the E. E. Salpeter (1955) IMF, therefore, we apply a multiplicative factor of 0.64 to convert it to the G. Chabrier (2003) IMF used in this work. Fig. A1 shows this comparison using the PROSPECTOR-inferred Hα fluxes for galaxies with $8.0 \leq \log(M_\star/M_\odot) \leq 10.3$ (grey), and using the fluxes measured with NIRSpec (purple, as seen in Fig. 2). As can be see, there is an overall agreement between SFR_{10} and $SFR_{H\alpha}$.

APPENDIX B: MIRRORING DISTRIBUTIONS

Figure B1 shows the process of mirroring non-Gaussian distributions of Δ_{MS} for $sSFR_{10}$, described in Section 5.1.
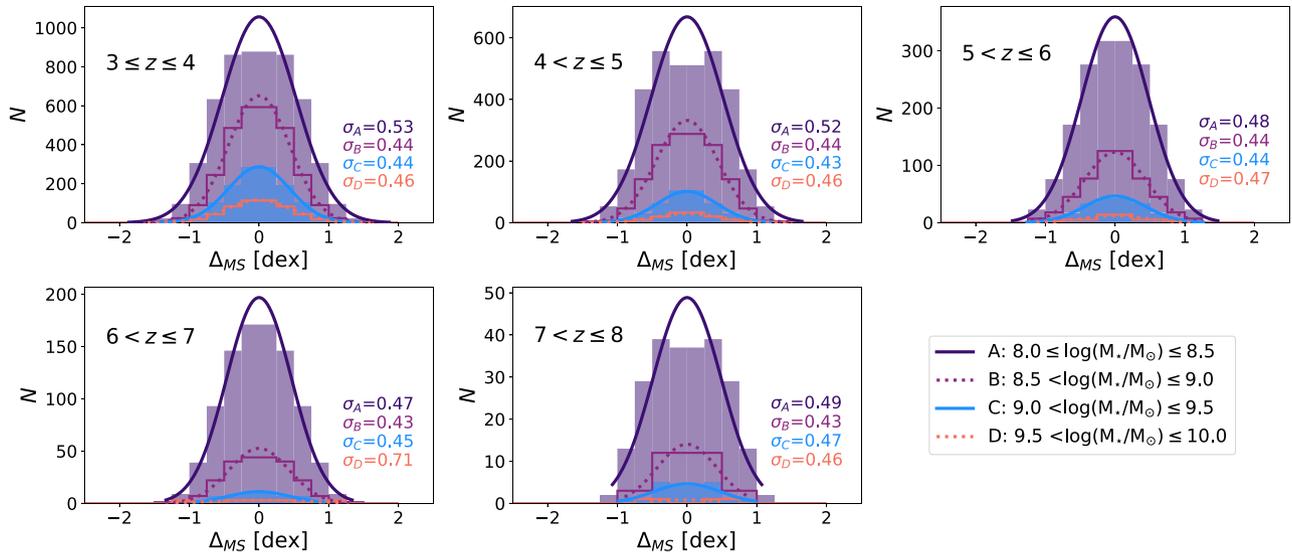
Figure B1. Same as in Fig. 8, but mirrored around zero, in order for them to be described by Gaussian distributions. The standard deviation for each mass bin is shown for each panel, labelled according to the legend (in each panel, the number of galaxies decreases as stellar mass increasesThis scatter represents the median observed scatter, $\sigma_{\rm obs}$ (i.e. includes scatter introduced by the SED-fitting routine). We note that for a given mass bin, $\sigma_{\rm obs}$ does not show a strong evolution with redshift.

APPENDIX C: STAR FORMATION HISTORIES RETRIEVAL TESTS

To assess the limitations of PROSPECTOR when retrieving SFHs, and consequently, SFRs, we use as input the best-fitting photometry of two galaxies in our sample with no recent star formation, low stellar mass ($\log(M_\star/M_\odot) \approx 7.5$), and at the extremes of our redshift range ($z = 3.00$ and 8.35). The input photometry and SFHs used are shown in Fig. C1. The objective of this test is to confirm that PROSPECTOR can retrieve SFHs and SFRs reliably at low stellar masses (below the stellar mass completeness limit derived in Section 3.2).

We define three cases for each galaxy, depending on the number of photometric bands used in the fitting routine: (a) all *HST* and *JWST* bands potentially available in our data, (b) all *JWST* bands that are potentially available, including both medium and wide bands, and (c) only *JWST* wide bands.

In Figs C2 and C3, we show the output SFHs for the cases described above, for $z = 3.00$ and 8.35, respectively. It can be seen that at both redshifts, the output SFHs reproduce the shape of the input SFHs. In turn, this means that the stellar masses and SFR_{10} are also well retrieved. Importantly, this behaviour remains true as we reduce the number of photometric bands used as input. Although, as expected, the error bars increase when less information is available. With this simple test, we conclude that PROSPECTOR can indeed retrieve low SFRs at all the redshifts studied in this work, for galaxies with low stellar masses. Moreover, it can retrieve them reasonable well even in cases where no medium-band observations are available.
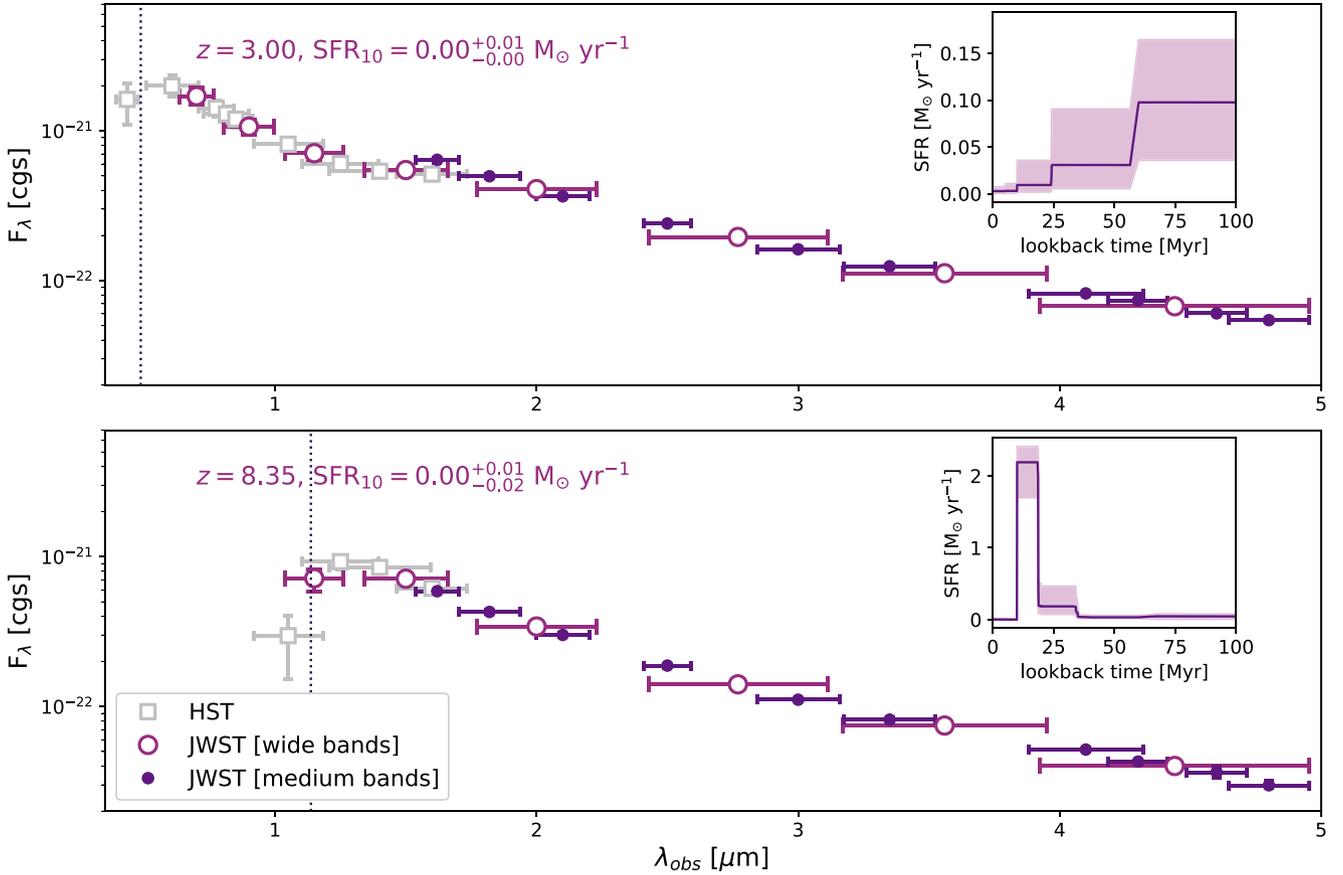
Figure C1. Input photometry and SFHs for two galaxies with $\log(M_\star/\mathrm{M}_\odot) \approx 7.5$, with no recent star formation, at $z = 3.00$ (top) and $z = 8.35$ (bottom), respectively. The different markers show photometry from *HST* (squares) and *JWST* wide (larger open circles) and medium (smaller filled circles) bands. We include the redshifted wavelength of Lyα for reference as a vertical dotted line.
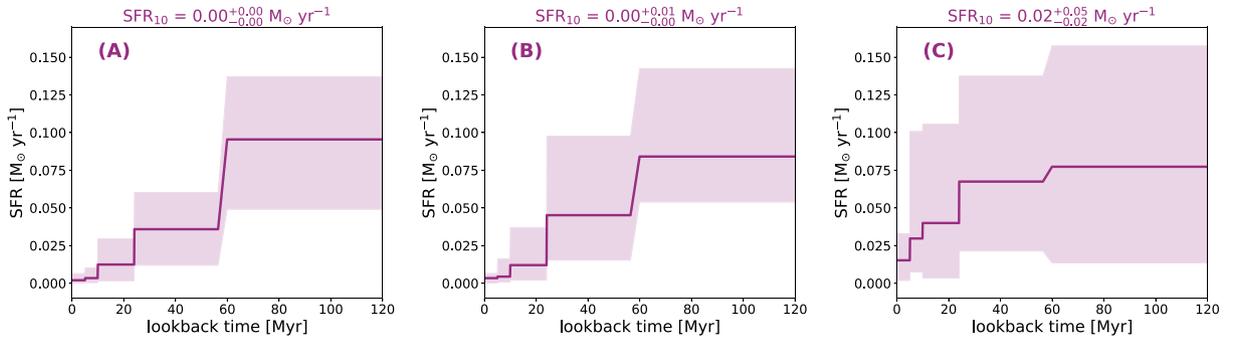
Figure C2. Retrieved SFHs for a galaxy with no recent star formation, at $z = 3$, and stellar mass of $\log(M_\star/\mathrm{M}_\odot) = 7.5$. The output SFR_{10} is given in the title of each panel. From left to right, the panels show cases with decreasing amount of photometric information: (a) all *JWST* and *HST* bands, (b) *JWST* medium and wide bands, and (c) *JWST* wide bands only. In all cases, PROSPECTOR is able to reliably retrieve the shape of declining input SFH, albeit with increasing error bars, which reflect the amount of input information.
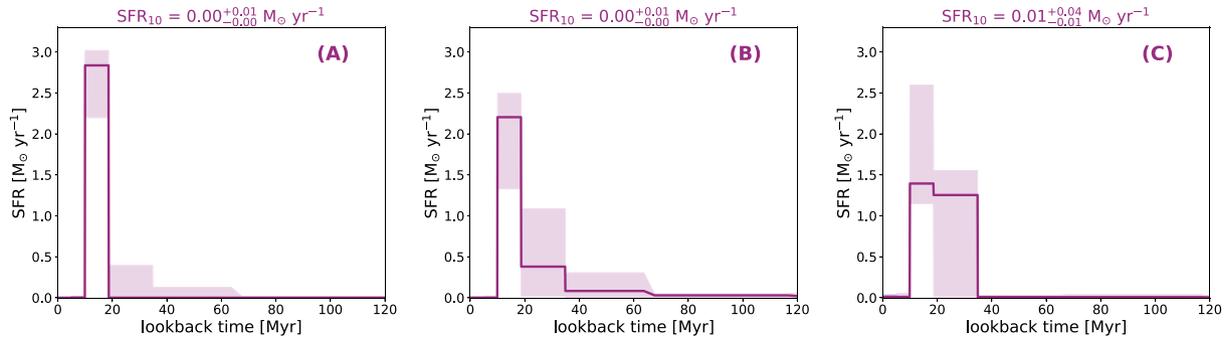
Figure C3. Same as Fig. C2, but for a galaxy at $z = 8.35$.

[1]*The Kavli Institute for Cosmology (KICC), University of Cambridge, Madingley Road, Cambridge CB3 0HA, UK*

[2]*Cavendish Laboratory, University of Cambridge, 19 JJ Thomson Avenue, Cambridge CB3 0HE, UK*

[3]*Centre for Astrophysics Research, Department of Physics, Astronomy and Mathematics, University of Hertfordshire, Hatfield AL10 9AB, UK*

[4]*Steward Observatory, University of Arizona, 933 N. Cherry Avenue, Tucson, AZ 85721, USA*

[5]*Center for Astrophysics | Harvard & Smithsonian, 60 Garden St., Cambridge, MA 02138, USA*

[6]*Department of Astronomy and Astrophysics, The University of Chicago, Chicago, IL 60637, USA*

[7]*Kavli Institute for Cosmological Physics, The University of Chicago, Chicago, IL 60637, USA*

[8]*Enrico Fermi Institute, The University of Chicago, Chicago, IL 60637, USA*

[9]*Department of Astronomy and Astrophysics University of California, Santa Cruz, 1156 High Street, Santa Cruz, CA 96054, USA*

[10]*NRC Herzberg, 5071 West Saanich Rd, Victoria, BC V9E 2E7, Canada*

[11]*DARK, Niels Bohr Institute, University of Copenhagen, Jagtvej 155A, DK-2200 Copenhagen, Denmark*

[12]*Institute of Astronomy, University of Cambridge, Madingley Road, Cambridge CB3 0HA, UK*

[13]*European Space Agency (ESA), European Space Astronomy Centre (ESAC), Camino Bajo del Castillo s/n, E-28692 Villanueva de la Cañada, Madrid, Spain*

[14]*Department of Physics, University of Oxford, Denys Wilkinson Building, Keble Road, Oxford OX1 3RH, UK*

[15]*Scuola Normale Superiore, Piazza dei Cavalieri 7, I-56126 Pisa, Italy*

[16]*European Southern Observatory, Karl-Schwarzschild-Strasse 2, D-85748 Garching, Germany*

[17]*Department of Physics and Astronomy, University College London, Gower Street, London WC1E 6BT, UK*

[18]*Department of Astronomy, University of Wisconsin-Madison, 475 N. Charter St., Madison, WI 53706, USA*

[19]*Centro de Astrobiología (CAB), CSIC-INTA, Ctra. de Ajalvir km 4, Torrejón de Ardoz, E-28850, Madrid, Spain*

[20]*NSF's National Optical-Infrared Astronomy Research Laboratory, 950 North Cherry Avenue, Tucson, AZ 85719, USA*

This paper has been typeset from a TeX/LaTeX file prepared by the author.